Journal of Photonics for Energy

PhotonicsforEnergy.SPIEDigitalLibrary.org

Plasmonic electrodes for bulk-heterojunction organic photovoltaics: a review

Christopher E. Petoukhoff
Zeqing Shen
Manika Jain
AiMei Chang
Deirdre M. O'Carroll

SPIE.

REVIEW

Plasmonic electrodes for bulk-heterojunction organic photovoltaics: a review

Christopher E. Petoukhoff,[a,*] Zeqing Shen,[b] Manika Jain,[a] AiMei Chang,[a] and Deirdre M. O'Carroll[a,b,c,*]

[a]Rutgers University, Department of Materials Science and Engineering, 607 Taylor Road, Piscataway, New Jersey 08854, United States

[b]Rutgers University, Department of Chemistry and Chemical Biology, 610 Taylor Road, Piscataway, New Jersey 08854, United States

[c]Rutgers University, Institute for Advanced Materials, Devices and Nanotechnology, 607 Taylor Road, Piscataway, New Jersey 08854, United States

Abstract. Here, we review recent progress on the integration of plasmonic electrodes into bulk-heterojunction organic photovoltaic devices. Plasmonic electrodes, consisting of thin films of metallic nanostructures, can exhibit a number of optical, electrical, and morphological effects that can be exploited to improve performance parameters of ultrathin photovoltaic active layers. We review the various types of plasmonic electrodes that have been incorporated into organic photovoltaics such as nanohole, nanowire, and nanoparticle arrays and grating electrodes and their impact on various device performance parameters. The use of plasmonic back electrodes can impact device performance in a number of ways because the mechanisms of performance improvements are often a complex combination of optical, electrical, and structural effects. Inverted bulk heterojunction device architectures have been shown to benefit from the multifunctionality of plasmonic back electrodes as they can minimize space-charge effects and reduce hole carrier collection lengths in addition to providing improved light localization in the active layer. The use of semi-transparent plasmonic electrodes can also be beneficial for organic photovoltaics as they can exhibit a variety of optical properties such as light scattering, light localization, extraordinary transmission of light, and absorption-induced transparency, in addition to providing an alternative to metal oxide–based transparent electrodes. [DOI: 10.1117/1.JPE.5.057002]

Keywords: plasmonic; electrode; bulk-heterojunction; organic; photovoltaic.

Paper 14074MV received Oct. 3, 2014; accepted for publication Nov. 10, 2014; published online Feb. 5, 2015.

1 Introduction

Surface plasmon resonances that exist on the surface of highly conductive, nanostructured metals have been shown to be of benefit to thin-film, inorganic photovoltaics[1–9] as well as organic photovoltaics.[10–15] Metals that are efficiently able to support surface plasmons in the visible regime (e.g., Ag, Cu, and Au) tend to have high work functions (either for the pure metal or with a native surface oxide), making them suitable anodes for inverted bulk-heterojunction organic photovoltaics (BHJ-OPVs) due to their more stable anodic behavior (see Fig. 1).[16,17] In this paper, we will review recent work on the incorporation of plasmonic electrodes, which are metal electrodes composed of an array of metallic nanostructures, into BHJ-OPV devices, with an emphasis on the inverted architecture. As such, plasmonic electrodes used as back and/or

*Address all correspondence to: Christopher E. Petoukhoff, E-mail: c.petoukhoff@rutgers.edu or Deirdre M. O'Carroll, E-mail: ocarroll@rutgers.edu

This review manuscript is also part of the section on "Breakthroughs in Photonics and Energy," highlighting primarily recent advances in the last three years.

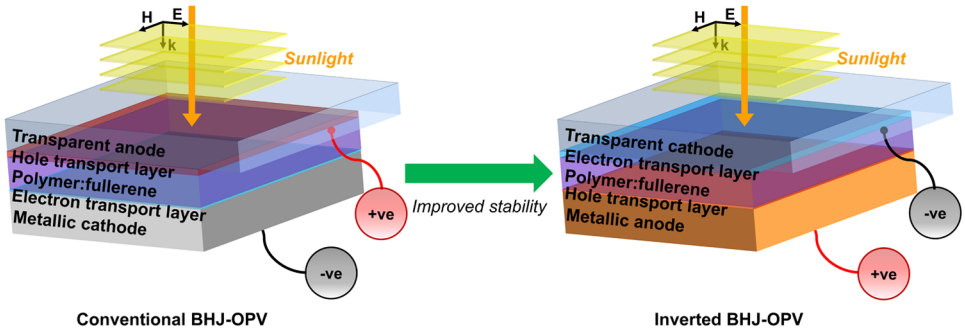

Fig. 1 Schematics of typical conventional and inverted bulk-heterojunction organic photovoltaic (BHJ:OPV) device architectures. Note that for conventional devices, the metallic cathode requires low work function metals such as Ca or Mg, or the use of electron transport layers, such as LiF/Al. For inverted devices, the metallic anode requires high work function metals such as Au, Cu, or Ni, or the use of hole transport layers, such as native metal oxides (Ag_2O/Ag, CuO/Cu, NiO/Ni) or other transition metal oxides (MoO_3, V_2O_5, WO_3) as the back interlayer.

front electrodes of a photovoltaic device are proposed to potentially enhance the performance of inverted BHJ-OPVs through light trapping or localization in the thin-film active layer.[1,2,5,12,14,15] In addition to light management, plasmonic electrodes may be suitable replacements for transparent conducting electrodes when employed as the front electrode of the device. By control of the structure and surface work function of the plasmonic electrodes (either through partial oxidation or through application of an interfacial layer), both the optical and electronic properties of the plasmonic electrode can be tuned.

Conventional BHJ-OPVs tend to have low device operational lifetimes, predominantly due to instabilities of the interfaces between the organic layers and the electrodes.[18] The most common hole transport layer used in conventional BHJ-OPVs is PEDOT:PSS (see Appendix for list of abbreviations of OPV materials) which, due to the low pH of PEDOT:PSS dispersions, tends to corrode the tin-doped indium oxide (ITO) layer, the most commonly used transparent electrode.[19] Additionally, low work function metals are employed as the back electrode (cathode) of conventional devices for electron collection from the BHJ active layer; however, low work function metals tend to degrade in air due to metal oxide or other compound formation, resulting in an increase in the back electrode work function, making such metals unstable cathodes.[16–18,20] In the inverted device geometry, the transparent (front) electrode serves as the cathode and the metallic (back) electrode serves as the anode through selection of metals with a high work function (e.g., Au, Ni, and Cu) and/or use of suitable electron and hole transport layers on the respective electrodes (Fig. 1). Inverted devices eliminate the need for PEDOT:PSS as the hole transport layer in contact with ITO, and alternative hole transport layers are often used between the metallic electrode and the active layer. Additionally, since formation of a native metal oxide layer can increase the work function of the metallic electrode, a more efficient and stable inverted device can result due to the reduced barrier for hole collection from BHJ materials and the inherent stability of higher work function electrode materials.[16,18] It has been shown that, whereas conventional OPVs may degrade to 80% of their initial power conversion efficiency within less than 1 day (unencapsulated), inverted BHJ-OPVs can last up to 40 days (in air) before degrading to 80% of their initial efficiency.[20] Over the past 5 years, for various BHJ active layers, the average power conversion efficiencies of inverted devices have ranged from values less than 1% up to ~4%,[16,21–24] while conventional OPVs have reached efficiencies ranging (on average) from 1% to ~6%[16,21] (with values reaching as high as 10.7% for a single junction OPV[25] and 12% for a multijunction cell[26]). However, in some cases, inverted OPVs have been shown to outperform conventional devices. He et al. recently reported a high-efficiency inverted device with an active layer consisting of PTB7:PC_{70}BM having an efficiency of 9.15% (compared to the conventional configuration using the same active layer, which had an efficiency of 8.24%).[27]

Nanostructured metallic electrodes can support surface plasmon resonances—strongly coupled light-surface charge density oscillations—and can either be localized (i.e., localized surface plasmon resonances, LSPRs) or delocalized propagating modes (also called surface

plasmon polaritons, SPPs).[1,2,28] In the case of a discrete metallic nanoparticle (NP), the oscillating electric field associated with light can displace the sea of electrons on the surface of the metal, forming an electric dipole on the metal [Fig. 2(a)].[1,2,28] The oscillating electric dipole on the surface of the metal gives rise to large localized electric field intensity enhancements, which can result in an increased photo-induced generation rate of excitons in the active layer of a BHJ-OPV.[1,2,4,5,29] Propagating SPPs, which can be excited at the interface between a dielectric or semiconductor and a continuous metallic film, undergo a similar phenomenon as LSPRs except the resonance is delocalized across the metal surface [Figs. 2(b) and 2(c)]. SPPs thus travel across the metal surface but are confined to the interface between the metal and surrounding dielectric/semiconductor medium. In contrast to metallic NPs dispersed into BHJ-OPVs, nanostructured metallic electrodes typically support some combination of LSPRs, SPPs, and hybridized modes.[14,15,30–32]

Plasmonic nanostructures are particularly relevant for thin-film photovoltaics (PVs), which tend to absorb less light (due to the nature of thin films) and often require novel nanophotonic light-trapping techniques to achieve reasonable efficiencies. Plasmonic nanostructures can be incorporated into BHJ-OPVs either by forming metallic nanostructured electrodes or interlayers or by embedding metallic NPs into one of the layers of the device. In this review, we will focus on the optical, electrical, and morphological effects of nanostructured plasmonic electrodes in BHJ-OPV devices. We will not review the plasmonic effects of discrete metallic NPs distributed

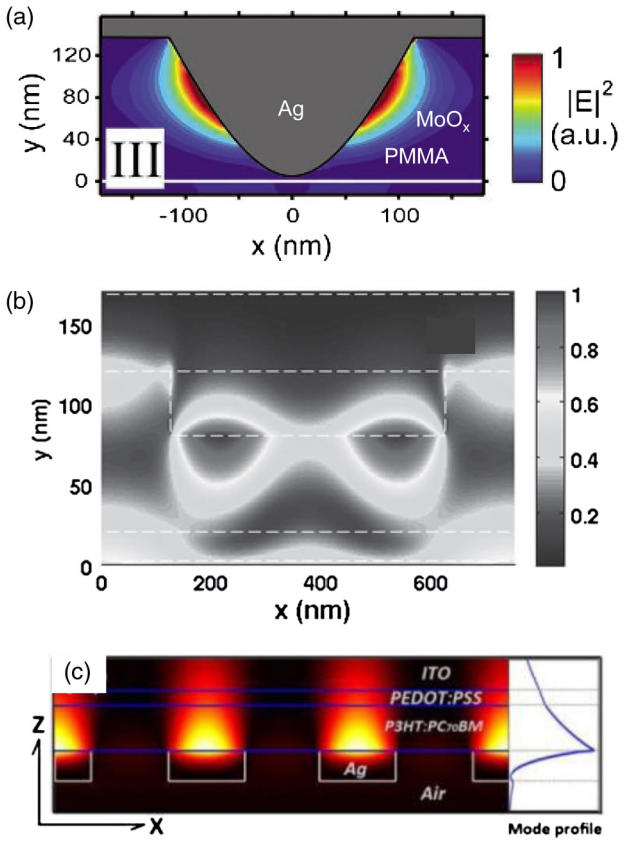

Fig. 2 Electric and magnetic field profiles for surface plasmon resonances. (a) Time-averaged electric field intensity ($|E|^2$) distribution, showing that localized surface plasmon resonances (LSPRs) can have strongly enhanced electric fields near the surface of the nanostructure, leading to enhanced absorption near these electromagnetic "hot spots."[33] (b) Time-averaged magnetic field amplitude ($|H_y|$) distribution, showing that surface plasmon polaritons (SPPs) can hybridize with Bloch modes in a metallic grating structure to greatly enhance the optical path length in the OPV.[32] (c) Time-averaged magnetic field intensity ($|H_y|^2$) distribution at the SPP resonance wavelength from a nanohole array; the spatial mode profile is plotted in the right panel of (c).[34] Figures reproduced with permission, courtesy of (a) Ref. 33, copyright 2013, Wiley; (b) Ref. 32, copyright 2012, Wiley; (c) Ref. 34, copyright 2010, OSA.

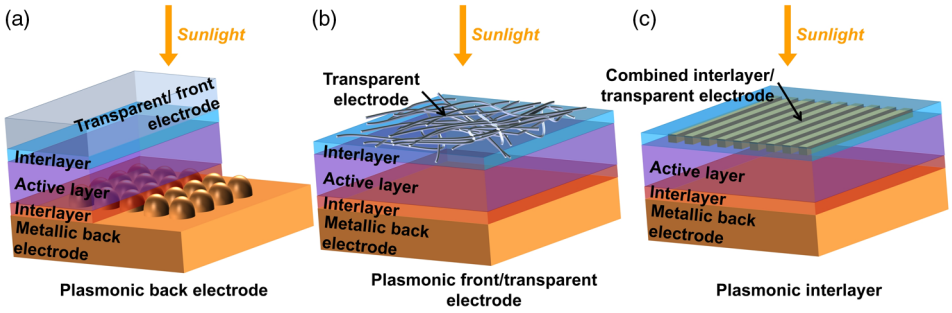

Fig. 3 Selected examples of plasmonic electrode architectures reported in the literature. (a) Plasmonic back electrodes consist of a nanostructured opaque metal electrode serving as the back reflector of the device. (b) Plasmonic front/transparent electrodes consist of metallic nanostructures forming a continuous transparent conductive network, such as silver nanowire meshes. (c) Plasmonic interlayers consist of continuous metallic nanostructures embedded in one of the interlayers (electron- or hole-transport layer), which, in some cases, can have a dual role as a both an interlayer and a front/transparent electrode.

into BHJ-OPV layers, as there are a number of recent reviews on this subject [e.g., (Refs. 10–15)]. There are three primary ways in which metallic nanostructured electrodes can be placed inside a PV device: (1) on the back metallic electrode;[31–42] (2) on the front/transparent electrode;[43–47] or (3) as a charge transport interlayer inside of the device stack[48–51] (see Fig. 3). Each of these configurations has different requirements for fabrication and can lead to enhancements in the total absorption as well as in the device efficiency in different ways. Tables 1 to 3 show the enhancement factors for BHJ-OPV devices incorporating plasmonic electrodes as back electrodes (Table 1), front electrodes (Table 2), or some combination of plasmonic electrodes and nanostructures (Table 3). Here, we will discuss the performance of plasmonic electrodes incorporated into BHJ-OPV devices in each of these configurations, as well as the optical, electrical, and morphological effects associated with them.

2 Plasmonic Back Electrodes

Nanostructuring the back metallic electrode is a common method employed to increase light trapping in the active layer of BHJ-OPVs. Patterns can be fabricated using large-area, nanofabrication methods such as nanoimprint lithography (NIL),[30,36,70,54] nanosphere lithography,[33,40] and nanotemplate-directed fabrication.[41,42] Roll-to-roll processes that incorporate NIL are currently under development and could enable high-throughput integration of plasmonic back electrodes.[71,72] We begin by discussing some of the fabrication methods for producing plasmonic back electrodes.

Metallic gratings have been extensively studied as the back electrodes of BHJ-OPVs for both inverted[30,31,36,52,54] and conventional[36–38,48,52,73–76] devices [Figs. 4(a)–4(c)]. One-dimensional (1-D) gratings have the benefit of relatively simple fabrication (e.g., laser interference,[39,75] NIL,[30–32,36,54,70,77,78] or solution-based fabrication via NP-imprinting[79]) and can couple light into both LSPR and propagating SPP modes. NIL is one of the most common approaches to fabricating metallic gratings as back electrodes as it is capable of fabricating large areas of nanoscale structures with great precision and low cost.[77,78] NIL is carried out by the direct mechanical deformation of a resist by applying a patterned mold under pressure at elevated temperatures[30,36,77,78] or with exposure to UV light.[80,81] It is considered a nonconventional lithography in that it can achieve a higher resolution (sub-25 nm structures) than traditional photolithography techniques since it is not limited by the effects of light diffraction and beam scattering.[70,77,78] 1-D metallic grating back electrodes have been fabricated by imprinting directly into the BHJ active layer blend, where the active layer served as the resist in the NIL process, [Fig. 4(a)][30–32,36] followed by subsequent metal deposition. In some instances, where it would have been deleterious to the active layer to use thermal or photocurable NIL, Li et al. developed and employed a vacuum-assisted NIL process,[32] in which NIL was conducted simply by applying a mold containing the nanostructures to the active layer and placing both in a vacuum chamber at

Table 1 Table of BHJ-OPV efficiency (η) enhancement factors for devices containing plasmonic back electrodes relative to planar devices ($\eta_{plasmonic}/\eta_{planar}$; actual $\eta_{plasmonic}$ values in brackets).

Geometry	Active layer system	EF (η) or (λ)[a]	T/E	Device type	Mechanisms	Ref
1-D Ag grating ($\Lambda = 140$ nm)	P3HT:PCBM	1.21 (int)[a]	T	Conv	Near-field enhancement	48
1-D Al grating ($\Lambda = 250$ nm)	P3HT:PCBM	2.72 (618 nm)[a]	E	MIM	SPP	39
1-D Ag grating ($\Lambda = 300$ nm)	PTB7:$PC_{70}BM$	1.04 (10.21%)	T	Inv	Improved absorption, but reduced charge separation	52
1-D Al grating ($\Lambda = 350$ nm)	P3HT:PCBM	0.89 (2.28%)	T	Conv	Increased generation rate, but reduced charge separation	38
1-D Ag grating ($\Lambda = 500$ nm)	PCDTBT:PCBM	1.10 (int)[a]	T	Coating	LSPR and SPP	53
1-D Ag grating ($\Lambda = 700$ nm)	PTB7:$PC_{70}BM$	1.07 (7.73%)	E	Inv	Waveguide modes, Wood's anomaly, and LSPR	31
1-D Ag grating ($\Lambda = 750$ nm)	P3HT:PCBM	1.19 (3.68%)	E	Inv	Diffraction and SPP	30
1-D Ag grating ($\Lambda = 750$ nm)	P3HT:PCBM	2.37 (1.73%)	E	Inv	Near-field enhancement, reduced recombination and space-charge accumulation	36
1-D Ag grating ($\Lambda = 750$ nm)	PBDTTT-C-T:$PC_{70}BM$	1.10 (8.38%)	E	Inv	Increased interface area, reduced R_s, Wood's anomaly, and SPP-Floquet mode hybridization	32
1-D Ag grating ($\Lambda = 1040$ nm)	P3HT:PCBM	1.15–1.25 (int)[a]	T+E	Conv	SPP and Fabry-Pérot resonance hybridization and waveguide modes	37
2-D Ag grating ($\Lambda = 350$ nm, $h = 55$ nm)	P3HT:PCBM	1.25 (3.85%)	E	Inv	Reduced R_s, polarization-insensitive LSPR	54
2-D periodic Ag nanohole array ($\Lambda = 320$ nm)	PCPDTBT:PCBM	2.12	T	Conv	Short range SPP	34
2-D periodic Al granualar structures ($\Lambda = 420$ nm)	PTPTBT:$PC_{70}BM$	1.10 (3.15%)	E	Conv	Back-scattering and LSPR	40
2-D quasi-periodic Ag hole array	P3HT:PCBM	7 (700 nm)[a]	E	Coating	Near-field enhancement	55
Multiperiodic Ag triangular grating	P3HT:PCBM	1.21 (int)[a]	T	Coating	SPP resonances, waveguide mode resonances, Fabry-Pérot modes, and scattering	56
Corrugated Ag film	P3HT:ICBA	1.06 (5.56%)	E	Inv	LSPR	33
AgNP monolayer ($d = 45$ nm; $h = 20$ nm)	P3HT:PCBM	2.4 (0.11%)	E	Inv	Back-scattering	57
AgNP array/Ag film	P3HT:PCBM	11 (740 nm)[a]	E	Coating	LSPR	41
Gap waveguide mode with vertically oriented polymer chains	P3HT	2.5 (int)[a]	T	Coating	Orientation-dependent SPP coupling	58

Note: Abbreviations used: EF = enhancement factor; λ = wavelength; d = diameter; h = height; Λ = period; T = theory; E = experiment; Conv = conventional; Inv = inverted; Coating = plasmonic electrode coated with active layer (incomplete device); MIM = metal-insulator-metal; Ref = reference.
[a]Denotes absorption EF occurring at the wavelength(s) specified in brackets; int = integrated absorption EF.

Table 2 Table of OPV efficiency (η) enhancements for devices containing plasmonic front electrodes relative to planar devices ($\eta_{plasmonic}/\eta_{planar}$; actual $\eta_{plasmonic}$ values in brackets).

Geometry	Active layer system	EF (η) or (λ)[a]	T/E	Device type	Mechanisms	Ref
1-D periodic Ag nanowire array ($\Lambda = 220$ nm, $lw = 55$ nm)	CuPc/C_{60}	1.38 (1.32%)	E	Conv	LSPR and waveguiding	49
1-D periodic Ag grating ($lw = 60$ nm; $\Lambda \sim 200$ nm)	CuPC/PTCBI	1.5 (int)[a]	T	Conv	Broadband SPP	50
2-D Ag grating ($\Lambda = 250$ nm)	CuPc/C_{60}	1.75 (J_{sc})	T	Conv	Coupled SPP between grating and back metal electrode and improved charge separation	59
2-D periodic Au hole array ($\Lambda = 200$ nm, $d = 175$ nm)	P3HT:PCBM	1.52 (4.4%)	E	Conv	Plasmonic cavity; reduced sheet resistance	45
Ag nanowire mesh ($l = 8.7$ μm, $d = 103$ nm)	CuPc/C_{60}	0.57 (0.63%)	E	Transp	Larger R_s, scattering	60
Ag nanowire mesh ($d = 25$ nm, $l > 10$ μm) on glass	PTB7-F20:$PC_{70}BM$	0.87 (5.80%)	E	Conv	Reduced sheet resistance, increased transmission	61
Ag nanowire mesh ($d = 25$ nm, $l > 10$ μm) on PET	PTB7-F20:$PC_{70}BM$	1.12 (5.02%)	E	Conv	Reduced sheet resistance, increased transmission	61
AZO-Ag-AZO multilayer electrode	P3HT:PCBM	1.57 (2.14%)	E	Conv	Reduced sheet resistance	62
AZO-Ag-AZO multilayer electrode	PTB7:$PC_{71}BM$	0.88 (6.1%)	E	Inv	Reduced transparency and non-ideal work function	63
ITO-Ag-ITO multilayer electrode	P3HT:PCBM	1.38 (3.25%)	E	Conv	Reduced sheet resistance, increased transmission	64
ITO-Cu-ITO multilayer electrode	P3HT:PCBM	1.62 (2.78%)	E	Conv	Reduced sheet resistance	65
GZO-Ag-GZO multilayer electrode	P3HT:PCBM	1.81 (2.84%)	E	Conv	Reduced sheet resistance	62
Ag microgrid ($lw = 40$ μm, $\Lambda = 640$ μm)	APFO-Green 5:PCBM	1.20 (1.00%)	E	Conv	Reduced sheet resistance	66

Note: Abbreviations used: EF = enhancement factor; λ = wavelength; d = diameter; Λ = period; lw = line width; l = length; J_{sc} = short-circuit current density; T = theory; E = experiment; Conv = conventional; Inv = inverted; Transp = semi-transparent OPV (2 transparent electrodes); Ref = reference.
[a]Denotes absorption EF occurring at the wavelength(s) specified in brackets; int = integrated absorption EF. Note that molecular bilayer heterojunction OPVs include active layer systems where the donor and acceptor are separate layers (separated in the text by a "/"), whereas in BHJ-OPVs, the donor and acceptor are one continuous composite layer (separated in the text by a ":").

10^{-2} Torr and room-temperature.[31,32] Alternatively, metallic grating electrodes have also been fabricated by depositing the active layer on top of a pre-patterned grating.[37,39,82] While directly imprinting the active layer can potentially change the molecular orientation or crystallinity of the active layer due to the application of pressure and/or high temperatures (see Sec. 2.3),[83,84] this potential morphological impact on device performance is not often characterized or accounted for.[30–32,36,54]

Two-dimensional (2-D) plasmonic electrodes can have additional benefits over 1-D grating electrodes, as discussed in the sections below, although they often require more fabrication steps than 1-D plasmonic electrodes. One type of 2-D nanostructured metallic back electrode employed in BHJ-OPVs is an array of nanoholes perforated into a metallic thin film [Fig. 4(i)].[34,35,55,69,86,87] In one study, various periodic nanohole arrays were patterned by focused ion beam (FIB) milling into a 300-nm-thick Ag film (see Sec. 2.1).[55] Although this type of study is very useful to gain an understanding of how periodicity affects absorption enhancements, the FIB nanofabrication route is not currently amenable to large-scale processing, which is a major drawback for

Table 3 Table of OPV efficiency (η) enhancements for devices containing combined plasmonic electrodes and nanostructures relative to planar devices ($\eta_{plasmonic}/\eta_{planar}$; actual $\eta_{plasmonic}$ values in brackets).

Geometry	Active layer system	EF (η) or (λ)[a]	T/E	Device type	Mechanisms	Ref
1-D Ag grating back electrode ($\Lambda = 750$ nm) + embedded Au NPs in the active layer ($d = 50$ nm)	PBDTTT-C-T: $PC_{70}BM$	1.16 (8.79%)	E	Inv	Larger interface area, improved electron and hole mobilities, reduced R_s, coupled LSPR-SPP-Floquet modes	32
Combined 1-D Ag grating back ($\Lambda = 200$ nm, $w = 30$ nm + front electrode ($\Lambda = 200$ nm, $w = 50$ nm)	CuPc/PTCBI	1.67 (int)[a]	T	Conv	Coupled SPP modes	67
Combined 1-D Ag grating back + front electrodes ($\Lambda = 490$ nm, $w = 60$ nm for each grating)	P3HT:PCBM	1.35 (int)[a]	T	MIM	Coupled LSPR + SPP, Bloch modes	68
Front Ag nanodisk array ($\Lambda = 100$ nm, $d = 30$ nm) + 2-D periodic Ag nanohole array ($\Lambda = 240$ nm, $d = 120$ nm) back electrode	P3HT:PCBM	1.83 (int)[a]	T	Conv	LSPR + SPP modes	69
Front Ag nanodisk array ($\Lambda = 160$ nm, $d = 80$ nm) + 2-D periodic Ag nanohole array ($\Lambda = 160$ nm, $d = 100$ nm) back electrode	CuPC/PTCBI	2.28 (int)[a]	T	Conv	LSPR + SRSPP modes	35

Note: Abbreviations used: EF = enhancement factor; λ = wavelength; d = diameter; Λ = period; w = width; int = integrated absorption; T = theory; E = experiment; Conv = conventional; Inv = inverted; MIM = metal-insulator-metal; Ref = reference.

[a]denotes absorption EF occurring at the wavelength(s) specified in brackets; int = integrated absorption EF. Note that molecular bilayer heterojunction OPVs include active layers where the donor and acceptor are separate layers (separated in the text by a "/"), whereas in BHJ-OPVs, the donor and acceptor are one continuous composite layer (separated in the text by a ":").

incorporating these structures into real devices. Other methods of fabricating nanohole arrays in metallic films exist and are described in Sec. 3.

Another class of 2-D nanostructured metallic electrodes explored for BHJ-OPVs is corrugated metal surfaces. In one example, wrinkles and folds were formed on an optical adhesive layer by biaxially induced stress from UV exposure followed by corona discharge, and the device was constructed on the corrugated epoxy surface,[85] giving each layer a textured corrugation [Figs. 4(d) and 4(e)]. Variations of nanosphere lithography[88,89] have also been used for creation of corrugated surfaces. For example, one study employed hole-mask colloidal lithography,[90–92] in which PS beads were drop cast onto the active layer, followed by deposition of MoO_x and subsequent removal of the PS beads.[33] This left behind an array of holes in the MoO_x; another 5 nm of MoO_x was deposited as a buffer layer in the pits of the holes, followed by 200 nm of Ag, resulting in a corrugated Ag electrode.[33] Another variation of nanosphere lithography was demonstrated by first creating a hole array by depositing PS spheres onto a Si substrate, partially etching the spheres using O_2 plasma, evaporating Ni onto the PS-coated substrate, removing the PS spheres, and inductively coupled-plasma etching into holes left behind by the spheres.[40] A negative copy of the hole array was formed using PDMS, which was then coated with P3HT:PCBM, and was finally transferred to a PEDOT:PSS/ITO substrate by stamping.[40] This left a 2-D, periodic hole array in the active layer, which was then coated with Al to form the corrugated metallic electrode by filling the holes in the active layer.[40] Finally, thermal evaporation of Ag through a nanoporous anodic aluminum oxide (AAO) membrane onto a metallic film has been used to create a randomly distributed 2-D array of AgNPs on a Ag film, which was then coated by the active layer by spin-coating[41,42] [Figs. 4(f)–4(h)].

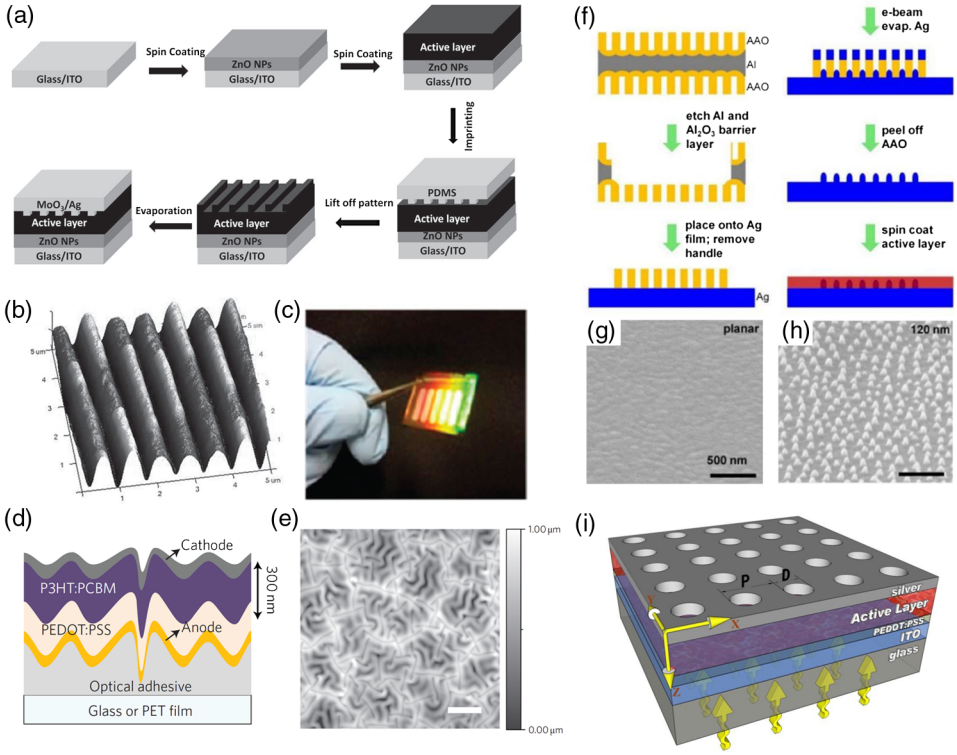

Fig. 4 Examples of plasmonic back electrode structures and fabrication methods. (a–c) Nanoimprinted active layer with 1-D metallic grating as a back electrode: (a) overview of a typical fabrication route for a grating-based OPV device; (b) AFM image of an imprinted PTB7:$PC_{70}BM$ film;[31] (c) photograph of a patterned device tilted to show the diffraction from the grating.[30] (d) and (e) Corrugated back electrode fabricated on an optical adhesive with wrinkles and folds: (d) schematic cross-section of a corrugated device; (e) AFM micrograph of a surface comprising of both wrinkles and folds formed in an optical adhesive film from high compressive stress. The scale bar is 5 μm.[85] (f–h) 2-D corrugated back electrode fabricated through template-directed deposition of AgNPs on Ag: (f) overview of the template-directed deposition of AgNPs on Ag with subsequent conjugated polymer active layer coating; (g) SEM micrograph of a planar Ag film; (h) SEM micrograph of AgNPs on a Ag film; scale bar, same as (g).[41] (i) 2-D periodic nanohole array as a back electrode.[34] Figures reproduced with permission, courtesy of (a and b) Ref. 31, copyright 2012, Wiley; (c) Ref. 30, copyright 2012, ACS; (d and e) Ref. 85, copyright 2012, Nature Publishing Group; (f–h) Ref. 41; (i) Ref. 34, copyright 2010, OSA.

2.1 *Optical Effects of Plasmonic Back Electrodes*

For 1-D metallic grating structures, phase-matching conditions can be achieved for coupling of light to a SPP when[28]

$$m\frac{2\pi}{\Lambda} = \pm\frac{2\pi}{\lambda}\left(\sqrt{\frac{\varepsilon_d\varepsilon_m}{\varepsilon_d+\varepsilon_m}} - \sin\,\theta_i\right), \tag{1}$$

where m is the diffraction order $(1, 2, 3, \ldots)$, Λ is the period of the grating, λ is the free-space wavelength, ε_d and ε_m are the complex dielectric functions of the surrounding dielectric (or semiconductor) and the metal, respectively, and θ_i is the angle of incidence of the excitation light. The incident excitation light should have an electric field component polarized perpendicular to the grating lines in order to couple into a grating mode (i.e., either unpolarized or transverse magnetic, TM, polarization).[12] It has been shown that, compared to TM polarization, for light polarized parallel to the grating lines (i.e., transverse electric, TE, polarization), there was considerably less absorption enhancement in an organic active layer-coated metallic grating relative to the same active layer material coated onto a planar metallic electrode.[39,53,56,82] Therefore, the performance of a 1-D metallic grating back electrode is highly sensitive to the

polarization of incident light, and for unpolarized sunlight, the observed enhancement factors in BHJ-OPV devices are less than what can be achieved for purely TM-polarized incident light [Fig. 5(a)]. This has been a large motivation for the use of 2-D metallic nanostructured electrodes, which tend to be far less sensitive to the incident light polarization state.[37,54,56] However, it is also possible to overcome polarization issues associated with 1-D gratings by employing 1-D gratings with large periods (>1000 nm), which can not only couple SPPs with Bloch modes [see below and Fig. 2(b)] but can also excite a photonic waveguide mode under TE polarized illumination, thereby allowing for both an in-plane propagating TM-polarized plasmonic mode and an in-plane propagating TE-polarized photonic mode to contribute to increased light trapping in the active layer.[37]

The range of plasmonic and photonic modes that have been observed for 1-D metallic gratings used in BHJ-OPVs are Bloch (i.e., Floquet) mode-coupled SPPs [Fig. 2(b)],[30–32,36,39,82,56] Wood's anomaly,[31,32] LSPRs [Fig. 2(a)],[31,53] back-scattering [Figs. 5(c)–5(g)],[31,53] and Fabry–Pérot resonances for triangular[56] and large-period gratings.[37] For excitation of Bloch mode-coupled SPPs, TM-polarized incident light was used in order to observe the effect in BHJ-OPV devices. Incident angle-insensitive absorption enhancement has been observed theoretically for a 1-D triangular grating structure.[56] The non-dispersive absorption enhancement was achieved by tuning "bright" and "dark" SPP modes, i.e., modes that were present for $\theta_i = 0$ and those that required $\theta_i > 0$. Tuning the grating height and fill factor (FF, base

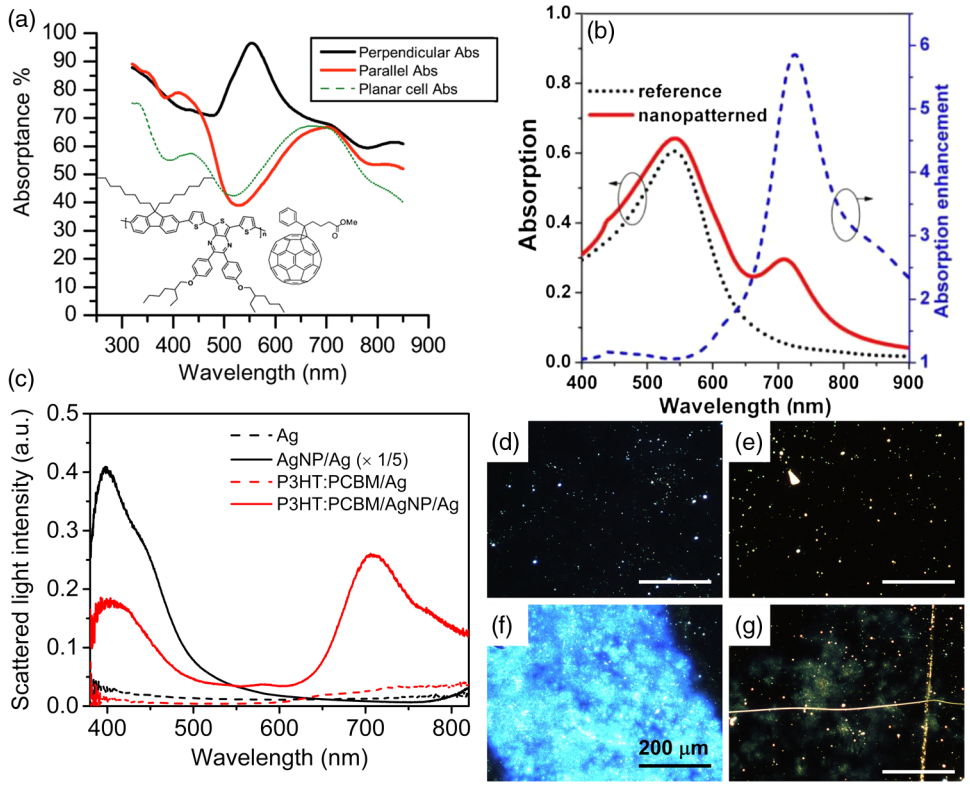

Fig. 5 Possible optical mechanisms for enhancing OPV device efficiency in the presence of plasmonic back electrodes. (a) Absorptance is highly dependent on polarization due to the transverse magnetic (TM) nature of surface plasmons; the chemical structure of APFO Green5:PCBM is shown in the inset.[82] (b) Calculated active layer absorption for a Ag nanohole array plasmonic back electrode with P3HT:$PC_{70}BM$ as the active layer.[34] (c) Resonant scattering can occur from arrays of AgNPs ($d = 100$ nm; $h = 120$ nm) on a Ag film (AgNP/Ag); the scattered light spectral response changes upon coating the AgNP/Ag with a P3HT:PCBM thin film. Dark-field scattered-light images are shown for the bare planar Ag (d) and AgNP/Ag (f) electrodes as well as for the P3HT:PCBM-coated planar Ag (e) and AgNP/Ag electrodes (g). The scale bars in (d,e,g) are the same as that in (f). Figures reproduced with permission, courtesy of (a) Ref. 82, copyright 2007, AIP; (b) Ref. 34, copyright 2010, OSA.

length of triangle divided by the period) were crucial to control the bright and dark modes.[56] By extending the simulations to a 2-D pyramid grating structure, the absorption enhancement became polarization-insensitive as well.[56]

Lu et al. integrated plasmonic 1-D Ag grating structures fabricated using NIL on the back electrodes of BHJ-OPV devices incorporating an active layer of PCDTBT:PCBM with two different thicknesses (30 and 60 nm).[53] They observed that the absorption enhancement factor decreased with increasing active layer thickness because a thinner active layer absorbs less light and, therefore, offers larger potential for absorption enhancement in the presence of plasmonic nanostructures. Additionally, the origin of the absorption enhancements was attributed to a combination of broadband scattering from the grating, LSPR modes near the active layer absorption edge, and SPP modes at wavelengths longer than the absorption band edge. It was shown that SPP modes were particularly sensitive to the active layer thickness and grating period due to requirements for phase matching. Parasitic absorption by the metallic gratings was also considered theoretically and was expected to account for a significant fraction of the experimentally measured absorption enhancement of the metallic grating and active layer composite structure,[53] which is a common issue associated with reporting absorption enhancement factors from experimental measurements.[33,37,39,41,42]

Sefunc et al. theoretically investigated the active layer optical absorption enhancement that occurred for a 1-D Ag grating back electrode (having a period of 140 nm) integrated into a conventional P3HT:PCBM-based BHJ-OPV device.[48] They compared the active layer absorption in a BHJ-OPV device incorporating the grating electrode to that of a planar BHJ-OPV for both TE and TM incident light polarizations and found that active layer absorption increased for both polarizations by up to ∼21% relative to the planar device configuration. The authors also reported that the performance of such grating electrodes exceeded that of similar gratings embedded in the PEDOT:PSS hole transport layer (i.e., a plasmonic interlayer).[48]

Other plasmonic back electrode structures, such as 2-D nanohole arrays in Ag, have resulted in broadband absorption enhancement experimentally[55,93] and computationally[34] in P3HT:PCBM films [Fig. 5(b)], particularly for thinner P3HT:PCBM films (∼24 nm thickness)[34,55,93] (Fig. 6). For thicker P3HT:PCBM films (150 nm), nanohole array back electrodes resulted in more modest absorption enhancement across the visible spectrum, with the strongest enhancement occurring for wavelengths longer than 600 nm, where the absorption coefficient of P3HT:PCBM is small [Figs. 5(b) and 6(a)].[34,55,93] A heptadeca-grid quasi-periodic nanohole array was predicted to be polarization- and angle-insensitive due to the broad, diffuse diffraction rings occurring in the Fourier transform power spectrum of the nanohole array [Fig. 6(b)] compared to the periodic points occurring in the Fourier transform power spectrum of a periodic nanohole array [Fig. 6(c)].[55] The quasi-periodic nanohole array was also further optimized computationally using a "cut and projection" algorithm in order to maximize the constructive interference between SPPs generated at each of the holes [Figs. 6(d) and 6(e)],[93] leading to an experimentally measured absorption enhancement factor of ∼6 at a wavelength of ∼700 nm [Fig. 6(a)]. Theoretical calculations of a periodic nanohole array in a Ag back electrode [Fig. 4(i)] have shown that integrated absorption enhancement factors can reach 2.12 for an optimized period of 320 nm by coupling light into a broadband short-range SPP (SR-SPP).[34]

Random arrays of AgNPs on Ag electrodes [Fig. 4(h)] have been shown to enhance OPVs predominantly through LSPR hot spots and backscattering into the active layer.[33,40–42] Although these 2-D corrugated metallic electrodes should theoretically be able to support SPPs at the interface between the polymer active layer and the metal films, this has not yet been demonstrated experimentally. P3HT:PCBM-based OPV device efficiency enhancement from corrugated metallic electrodes formed on wrinkles and folds [Figs. 4(d) and 4(e)] was shown not to arise from plasmonic effects, but was attributed to refraction of light at each interface of the folded and wrinkled device leading to improved light trapping and waveguiding within the photoactive layer.[85] Interestingly, this study also demonstrated significant external quantum efficiency (EQE) enhancement at wavelengths longer than the absorption edge of the P3HT:PCBM system (greater than 600% enhancement at wavelengths longer than 650 nm), which the authors suggested was due to either enhanced excitation of charge-transfer complexes or tail states of the P3HT and/or PCBM.[85] This type of electronic-state enhancement in the EQE beyond the bandgap wavelength of the polymer absorber can only be readily observed experimentally in functioning BHJ-OPV

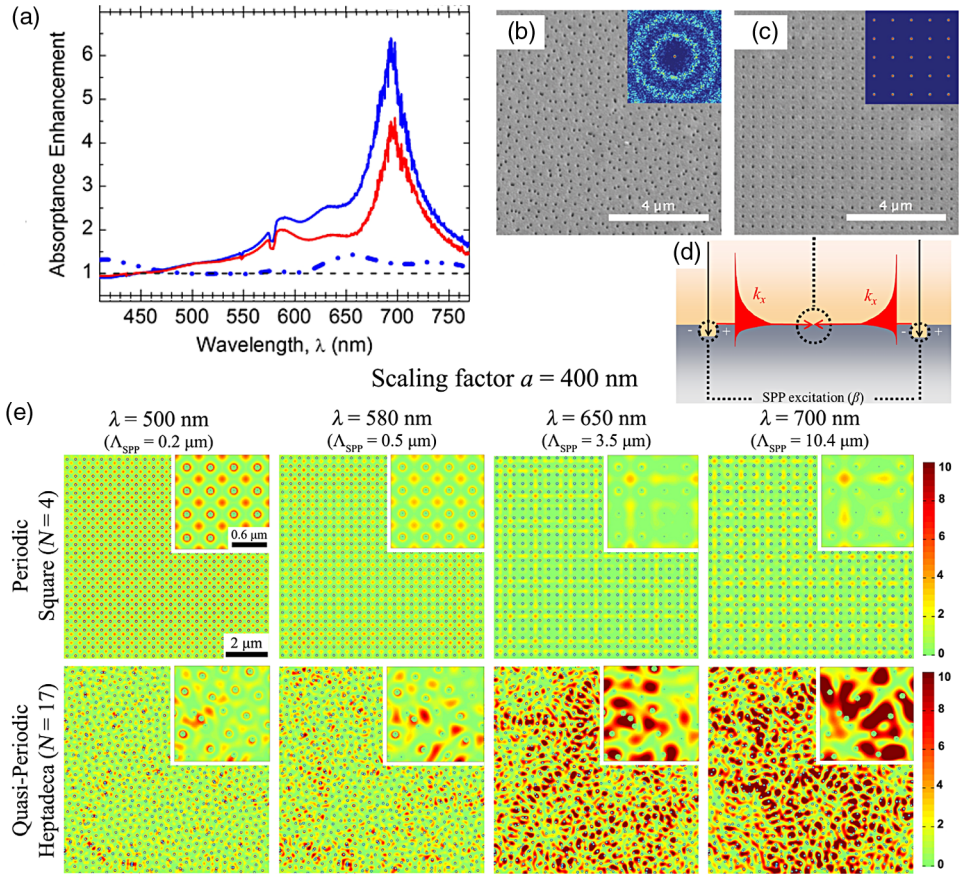

Fig. 6 Periodic and quasi-periodic nanohole arrays. (a) Experimental absorption enhancement comparison for a square periodic nanohole array (red curve) and a heptadeca quasi-periodic nanohole array (blue curve) with a P3HT:PCBM coating (24 nm in thickness); the blue dashed curve is for the quasi-periodic array with a thicker P3HT:PCBM coating (150 nm), and the black dashed curve shows an absorptance enhancement of 1, above which the absorptance in the P3HT:PCBM-coated nanohole array is greater than that of the P3HT:PCBM-coated planar Ag. All of the enhancement factors are relative to their planar equivalents (same thickness of P3HT:PCBM).[93] (b and c) SEM micrographs of a heptadeca quasi-periodic hole array (b) and a square periodic hole array (c); insets are the 2-D Fourier transform power spectra.[55] (d) Proposed mechanism for absorption enhancement using a nanohole array, where constructive interference from SPPs from neighboring holes can significantly increase the light intensity at the metal/dielectric interface. (e) Simulated 2-D electric field intensity distributions in square and heptadeca nanohole arrays at four different incident wavelengths, having a 24-nm thick P3HT:PCBM coating. The calculated SPP propagation length, Λ_{spp} is indicated above the 2-D field distributions for each wavelength.[93] Figures reproduced with permission, courtesy of (b and c) Ref. 55, copyright 2011, AIP; (a,d,e) Ref. 93, copyright 2013, OSA.

devices and is challenging to predict using optical simulations alone. This highlights the need for more extensive EQE studies of BHJ-OPV devices incorporating plasmonic electrodes because optical/photonic effects may not be the only cause of enhancements in solar power conversion efficiency.

2.2 *Electrical and Electronic Effects of Plasmonic Back Electrodes*

Although optical effects of plasmonic electrodes have been studied thoroughly, for both back and front electrodes, studies on how plasmonic electrodes can improve the electrical or electronic properties of BHJ-OPVs have been limited, especially for plasmonic back electrodes. Several studies employing 1-D metallic gratings on the back electrode have shown improved device FFs, which the authors attributed to the nanoimprinted active layer having a larger interfacial area

than the planar one, as well as the lower series resistance (R_s) of the nanoimprinted device.[30,32] While this could be due to the geometry of the grating structure alone, molecular orientation or crystallinity effects that may arise from directly imprinting the active layer were not considered in detail.[83,84] Such effects could give rise to increased charge mobility in the active layer, thereby reducing bulk recombination and R_s (see Sec. 2.3 on morphological effects).

However, a recent study has shown that the space-charge limit in OPVs can be overcome in devices incorporating metallic gratings.[36] This was attributed to the grating structure causing a redistribution of the local exciton generation in the active layer, thus giving a shortened transport path for positive charge carriers in inverted BHJ-OPV devices [Figs. 7(a), 7(b), 8(a), and 8(b)]. The authors suggested the resulting faster collection of holes at the plasmonic electrode reduced the bulk recombination and hole accumulation, as supported by photovoltage measurements [Figs. 8(c)–8(f)].[36] The grating structure was shown to be more useful for the inverted device architectures, where holes are collected at the metallic grating and electrons at the transparent, flat electrode [see Figs. 7(b) and 8].[36] These experiments indicate that electrical effects play an important role in designing plasmonic electrodes for BHJ-OPVs.

Coupled optical and electrical simulations have been performed for plasmonic-enhanced inorganic photovoltaics,[29] but to date, relatively few such studies have been carried out for plasmonic-enhanced BHJ-OPVs. In some reports, coupled optical and electrical simulations of metallic grating back electrodes for BHJ-OPVs have shown that, in general, optical absorption enhancements tend to be canceled out by electrical charge separation reductions.[38,52] However, it has been stressed that inverted OPVs can benefit more from grating electrodes because, in a planar OPV, the generation of excitons is highest towards the front electrode[38,52] [anode in a conventional device; cathode in an inverted device; see Figs. 1 and 7(a)]. Since holes typically have lower mobilities in polymers than electrons in the fullerenes, in the inverted configuration, the holes have a much longer path to travel to reach the metallic anode, leading to increased hole recombination in inverted devices relative to conventional devices [Fig. 7(a)]. The presence of the grating back electrode [or potentially any of the plasmonic back electrode

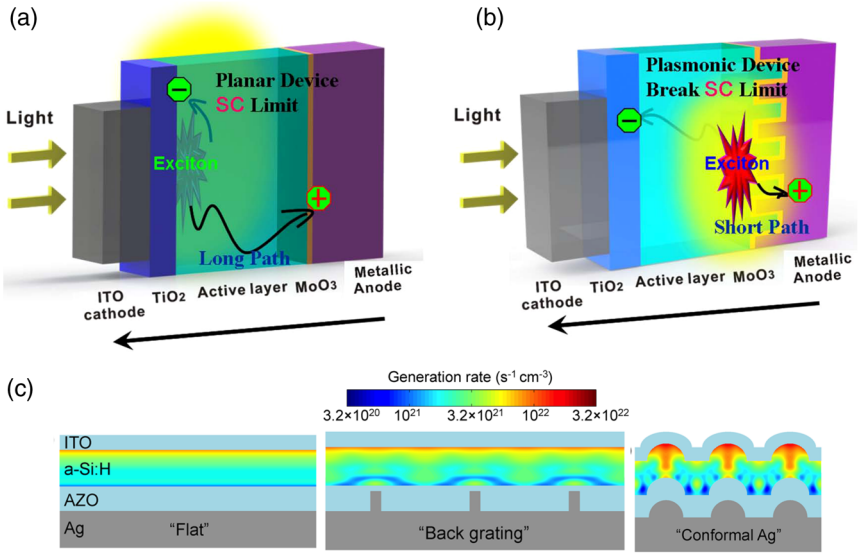

Fig. 7 Possible electrical mechanisms for enhancing OPV device efficiency in the presence of plasmonic electrodes. (a,b) Photogenerated excitons must dissociate, and subsequently, charge carriers must diffuse to their respective electrodes. Hole carrier diffusion length can be long in the inverted, planar configuration (a), but the hole carrier diffusion length can be significantly shortened when a grating is introduced to the back electrode of an inverted device (b).[36] (c) The reduced hole carrier diffusion length is partly due to the spatially modified generation rate of electron-hole pairs by the presence of the nanostructures. As examples, spatially modified generation rate distributions are shown for three different back metallic electrode configurations for an amorphous Si solar cell.[29] Figures reproduced with permission, courtesy of (a and b) Ref. 36, copyright 2014, Nature Publishing Group; (c) Ref. 29, copyright 2012, ACS.

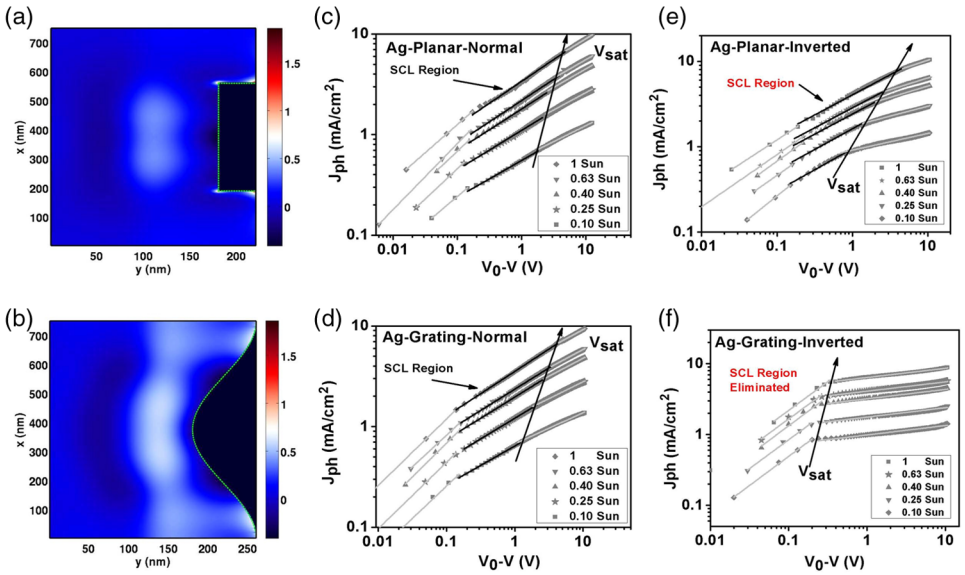

Fig. 8 (a and b) Abnormal exciton generation obtained from simulations. The profiles show the exciton generation rate enhancement of Ag-grating-inverted devices relative to Ag-planar-inverted devices for equivalent active layer thicknesses. The unpolarized results are shown for (a) a square grating and (b) a sinusoidal grating. (c–f) Space charge limit (SCL) characteristics for (c,d) conventional (i.e., normal) OPVs and (e and f) inverted OPVs measured at room temperature: (c) and (e) are for planar conventional and inverted devices, respectively; (d) and (f) are for, respectively, conventional and inverted devices incorporating a 1-D Ag grating back electrode. The plots show photocurrent versus effective applied voltage ($V_0 - V$) at different light intensities. The black lines in (c–e) indicate the dependence of photocurrent on the square-root of effective applied voltage (the expected behavior for photocurrent in the SCL region). Figure reproduced with permission, courtesy of Ref. 36, copyright 2014, Nature Publishing Group.

structures discussed here; see Fig. 7(c)] modifies the generation rate in the active layer, allowing for the holes to have a shortened path to the back plasmonic anode [Fig. 7(b)]. The elimination of the space-charge limited region in the grating-inverted OPV was the first experimental evidence that these plasmonic electrodes can have an effect on the charge carrier transport properties in BHJ-OPVs,[36] highlighting the importance of coupled optical and electrical experiments and simulations for designing effective plasmonic electrodes for use in BHJ-OPVs.

Another unique electronic effect that has not yet been explored for plasmon-enhanced BHJ-OPV devices, but is, regardless, a very active area of research for plasmon-enhanced PVs, is hot carrier generation and extraction at a metal nanostructure-semiconductor interface.[94–99] As mentioned in Sec. 2.1, parasitic absorption by the metal is often a common problem when employing metallic nanostructures for PV applications. Instead of losing the energy absorbed by the metal to heat, it is desirable to find an approach for generating electricity from that energy. For a metal-semiconductor non-Ohmic interface, a Schottky barrier exists, which is typically a smaller energy compared to the bandgap of the semiconductor.[94–99] When the metal absorbs light, an electron in the metal can be excited above the Fermi level (i.e., a "hot electron,"), leaving behind a "hot hole," and, if the energy of the incident light is greater than that of the Schottky barrier, the hot electron (hole) can be injected into the conduction (valence) band of the *n*-type (*p*-type) semiconductor, a process called internal photoemission.[94–99] In this way, sub-bandgap light can be absorbed by the device. Although the process is usually very inefficient for a typical metal-semiconductor interface,[94,95] employing the strong plasmonic absorption by metallic nanostructures can increase the hot carrier density, leading to greatly enhanced internal photoemission efficiencies.[95] This phenomenon has been studied for Si[94] and metal oxides,[95–97] but has not yet been investigated for organic semiconductors. The generation and extraction of hot electrons or holes could be investigated in BHJ-OPV devices employing plasmonic electrodes, as a possible means to harness sub-bandgap incident light energies or parasitic absorption by the metal that would otherwise be wasted.

2.3 *Morphological Effects of Plasmonic Back Electrodes*

A recent theoretical study has addressed the important issue of polymer chain morphology in coupling highly anisotropic SPP waves into anisotropic polymer absorbers.[58] Since single-interface SPPs have a strong out-of-plane component of the electric field, the largest absorption enhancement can be observed when the polymer chains align such that their transition dipole moment is oriented out-of-plane [i.e., in the "vertical" orientation, Fig. 9(c)].[58] While most conjugated polymers tend to have optical transition dipole moments oriented along the polymer backbone chain direction [hence, transition dipoles are typically in-plane due to the edge-on and face-on orientations that most conjugated polymers take during the solution-deposition process, Figs. 9(a) and 9(b)],[100–104] polymers such as PVK, with the conjugation occurring on the side group rather than the polymer backbone itself, satisfy the requirement for an out-of-plane transition dipole moment.[105] Additionally, polymer chains may align in the out-of-plane direction under certain circumstances, such as during electrochemical polymerization of P3HT in the vertically oriented pores of an AAO membrane, as evidenced by photoluminescence anisotropy studies.[106,107] Experimental studies of the effect of molecular orientation on SPPs generated at conjugated polymer–metal interfaces are currently lacking. Such studies could help to determine if control of molecular orientation can be used as an approach to further increase BHJ-OPV efficiency enhancement factors beyond those currently observed when incorporating electrodes that support surface plasmon modes.

As mentioned in the preceding sections, although the active layer is often imprinted directly prior to thermal evaporation to form a metallic grating, morphological studies (using, for example, wide-angle x-ray scattering), have not often been conducted in order to rule out contributions of improved crystallinity or molecular orientation to OPV device performance enhancements.[30–32] However, it has been shown that by imprinting the active layer directly, the orientation of the polymer molecules will be affected.[83,84] For example, imprinting a 1-D grating from a hard Si mold into neat P3HT led to an increase in the face-on to edge-on ratio, with the polymer backbones aligning preferentially along the direction of the grating's grooves.[84] Such morphological effects can have significant implications for polymer solar cells, since the face-on orientation has been suggested to have improved charge transport across the polymer-electrode interface.[84,108]

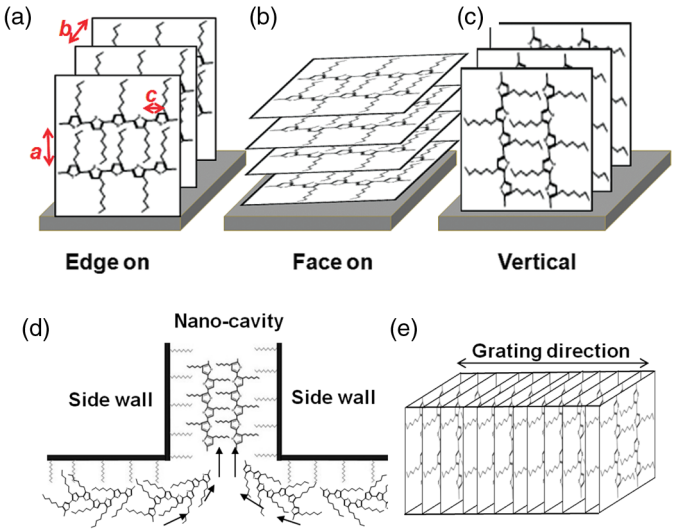

Fig. 9 Possible morphologies of conjugated polymer crystallites. (a-c) In general, there are 3 possible configurations in which polymer chains crystallize: (a) edge-on, with the polymer backbone parallel to the substrate and the side chains perpendicular; (b) face-on, with the polymer backbone and side chains parallel to the substrate; and (c) vertical, with the polymer chains perpendicular to the substrate and the side chains parallel. (d,e) Imprinting a P3HT thin film directly with a grating has been shown to modify the typical edge-on configuration in P3HT thin films to a more vertically oriented configuration, especially along the grating direction. Figure reproduced with permission, courtesy of Ref. 83, copyright 2009, ACS.

Additionally, vertical polymer chain alignment was shown to occur in another study in which different mold materials were used for the imprint pattern [Figs. 9(d) and 9(e)].[83] As mentioned above, vertical chain alignment could be useful for gaining further active layer absorption enhancement through alignment of the transition dipole axis of the polymer chains to the TM-polarized SPP electric fields. Therefore, these types of molecular orientation effects should be explored when directly imprinting the active layer for subsequent plasmonic back electrode formation.

3 Transparent Plasmonic Front Electrodes

Transparent electrodes are a critical component of BHJ-OPV devices, since they are required to simultaneously allow light to enter into the device, as well as to collect photogenerated electrons (inverted) or holes (conventional). Therefore, transparent electrodes must have a high transmittance, T, across the visible spectrum ($T \geq 90\%$) as well as have a low sheet resistance R_{sheet} ($\leq 10\ \Omega/\square$).[43] The most commonly used transparent electrodes in various photovoltaic and optoelectronic devices are doped metal oxides, especially ITO, which tends to be costly and brittle.[44,109,110] Novel transparent electrodes made by graphene,[111,112] carbon nanotubes,[113,114] and various nanostructured metals have been investigated in recent years as replacements for ITO. Among them, transparent metallic electrodes made from plasmonic metals (e.g., Ag, Au, Cu, Al) have attracted a lot of attention due to their unique optoelectronic properties. Some examples of metallic transparent front electrode structures are optically thin periodic nanohole arrays,[45,46,115,116] random nanohole arrays,[117] metallic gratings,[49,59,118–120] randomly distributed nanowire (NW) networks,[61,121–124] optically thin metal layers,[125–127] transparent conducting oxide (TCO)-metal-TCO multilayers,[62–65,128] and microgrid electrodes.[66]

The fabrication methods conventionally employed for metal films with periodic hole arrays have limited their widespread use as transparent electrodes. The fabrication of such structures has typically been carried out using focused ion beam milling[129–131] or electron-beam lithography,[132,133] techniques that are relatively expensive and time consuming. NIL,[45,134,135] interference lithography,[86] and nanosphere lithography[46,115,116] are all scalable, low-cost alternative techniques for fabricating periodic nanohole arrays [e.g., Fig. 10(a) and 10(b)] that could be employed in a roll-to-roll processing procedure as described earlier. The TCO-metal-TCO multilayers have been fabricated through sequential linear facing target sputtering for the TCO layers and thermal evaporation for the metal layer[62,64,65] and have typically used Ag as the metal,[62–65,128] although Cu has also been studied due to its lower cost and comparable conductivity to Ag.[65] Ag nanowires (AgNWs) are typically synthesized in solution and can exhibit atomically smooth surfaces with resistivities approaching that of bulk silver. As a result, AgNW meshes or networks are of great interest as transparent electrodes for solution-processed BHJ-OPVs on flexible substrates. Randomly distributed AgNW network electrodes [Fig. 10(e)] have been prepared by spin-coating,[61,136] drop-casting,[121] dip-coating,[137] Mayer rod-coating,[47,123] lamination,[122,60] and spray-depositing.[138–140] A recent progress report on metal NW networks has described in detail the current status of the field;[43] select optical, electrical, and morphological studies of these networks will be reviewed here. Transparent 1-D Ag grating electrodes [Figs. 10(c) and 10(d)] have also been prepared using NIL.[49] The techniques for preparing grating, AgNW or TCO-metal-TCO multilayer electrodes described here are all scalable, which is necessary for them to be of practical use in BHJ-OPV devices.

3.1 *Optical Effects of Plasmonic Transparent Electrodes*

Numerous examples of the use of metallic electrodes with nanohole arrays as transparent electrodes for optoelectronic devices have emerged in recent years. Chou et al. first reported building a "plasmonic cavity with subwavelength hole-array solar cell" (PlaCSH-SC), whose power conversion efficiency was 52% higher than their reference ITO-based solar cells (ITO-SC).[45] This PlaCSH-SC exhibited broadband absorption enhancement, leading to greater than 90% average absorption from 400 to 900 nm (compared to only 44% average absorption in the ITO-SC) as well as omniacceptance, i.e., having minimal dependence on polarization and incident angle.[45] The total reflectance from the PlaCSH-SC remained < 0.4 for all wavelengths, angles, and polarizations; for the ITO-OPV, the reflectance was strongly dependent on

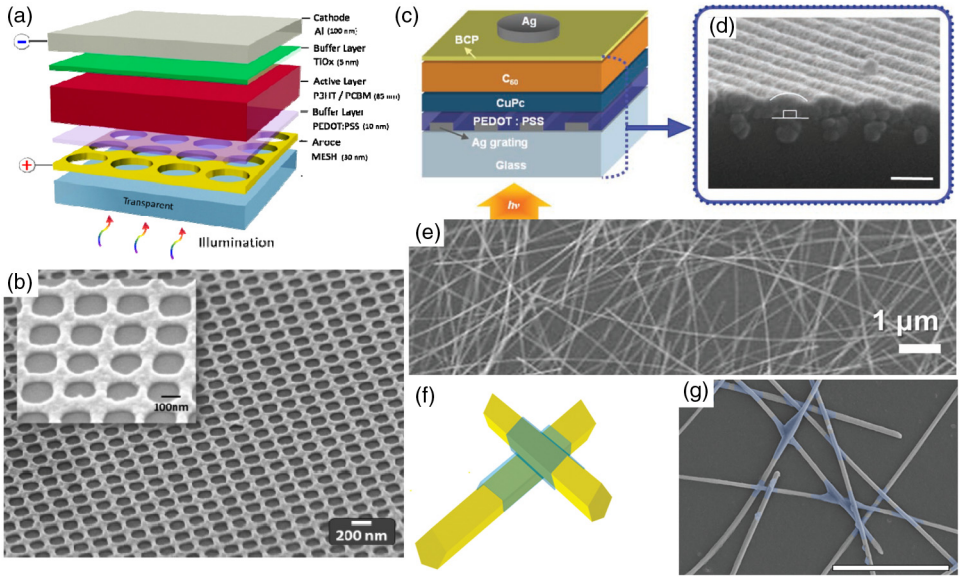

Fig. 10 Examples of plasmonic front/transparent electrodes. (a,b) Au metallic-mesh electrode with subwavelength hole array (MESH): (a) schematic of an OPV device incorporating a MESH front electrode (i.e., a PlaCSH-SC, see Sec. 3.1); (b) SEM micrograph of Au MESH electrode fabricated through large-scale nanoimprint lithography.[45] (c,d) 1-D Ag periodic grating front electrode: (c) schematic of OPV incorporating grating front electrode; (d) cross-sectional SEM micrograph of fabricated OPV device with the grating, but without the top Ag cathode. The scale bar is 200 nm.[49] (e–g) Ag nanowire mesh electrodes: (e) SEM micrograph of a Ag nanowire mesh;[61] (f) schematic of a PEDOT:PSS-soldered Ag nanowire junction; (g) SEM micrograph of PEDOT:PSS-soldered Ag nanowires (PEDOT:PSS is blue colored). The scale bar is 4 μm.[123] Figures reproduced with permission, courtesy of (a and b) Ref. 45, copyright 2013, OSA; (c and d) Ref. 49, copyright 2010, Wiley; (e) Ref. 61, copyright 2013, Wiley; (f and g) Ref. 123, copyright 2013, Wiley.

wavelength, incident angle, and polarization, reaching values between 0.5 and 1.0. For efficiently collected scattered light, the omniacceptance behavior of this PlaCSH-SC increased the efficiency enhancement to 175%, with a remarkable efficiency of 8% for a P3HT:PCBM-based device.[45] Chi et al. applied a similar periodic nanohole array in Al as a front electrode for conventional silicon solar cells and achieved an excess photocurrent density near 190% of the normal current density of a standard solar cell.[132] In addition, plasmonic electrodes consisting of nanohole arrays have also been used as transparent electrodes in organic light-emitting diodes (OLEDs). Ding et al. fabricated a novel PlaCSH-OLED with a 1.75-fold higher external quantum efficiency and light-extraction efficiency than a control ITO-OLED.[134] Moreover, this kind of structure was also proposed for use in surface-enhanced spectroscopy[141] and surface plasmon resonance sensing.[142,143] Although the periodicity of nanohole arrays plays a very important role in their plasmonic properties,[35,129,131,144] random nanoporous metal structures have also shown promising plasmonic properties and can be achieved by large-area dealloying methods.[145,146] However, this type of random nanoporous metal has not yet been employed in BHJ-OPV devices. Additionally, the particular photonic/plasmonic modes or optical mechanisms associated with periodic nanohole arrays that could contribute to optoelectronic device performance improvements have not yet been identified comprehensively.

An intriguing property of metallic electrodes with periodic nanohole arrays that could contribute to the optical mechanisms giving rise to absorption enhancement in OPVs is extraordinary optical transmission (EOT), which was first discovered by Ebbesen et al.[147] For EOT, it is believed that the incident light is first coupled into SPPs on the surface of the nanoporous metal film, then transmitted through the nanoholes and reradiated as light from the other surface, resulting in a higher transparency than predicted by traditional aperture theory.[129–131] Besides the higher transparency at certain wavelengths caused by this effect, the trapping and localization of light by SPPs on the surface of the film could increase the interaction time between the light

and the active layer in photovoltaic devices and thus improve the absorption efficiency. EOT was first observed for periodic hole arrays perforated in optically thick metal films (i.e., thickness greater than ~5 times the skin depth of the metal), whereby the incident light first coupled into SPPs on the front side, then propagated through the holes and reradiated as light via SPPs on the back side.[129–131,147,148] In this case, the SPPs on both sides of the perforated metal film were considered to be uncoupled.[149] It was shown that the transmission of hole arrays increased exponentially for decreasing Ag film thicknesses from 800 nm to ~350 nm while the EOT peak wavelength remained relatively constant.[149] Below these metal thicknesses, the transmission no longer increased exponentially with decreasing Ag film thickness and a red shift and broadening of the peaks in the transmission spectra were observed.[149,150] For such periodic hole arrays in optically thick metal films, although the transmission was greatly enhanced relative to the expected transmission as a result of EOT (transmission efficiency larger than unity[129]), the absolute transmittance of the structure was still too low for use as transparent electrodes (<20%).[129–131,147,148]

However, more recently, EOT in hole arrays in optically thin metal films (i.e., thicknesses less than 1 to 3 times the effective skin depth of the metal) has been investigated, although the EOT mechanism is slightly different compared to the thicker metal films due to the coupling of SPP modes on both side of the perforated film.[148–155] For optically thin metal films with periodic nanohole arrays, SPPs on both sides of the film interact before transmitting through the holes, giving rise to both long-range SPPs (LR-SPPs) and SR-SPPs.[34,148] In some studies, the transmission has been shown to be reduced relative to planar metal films of equivalent thicknesses.[153,154] However, although there is typically a dip in the transmission spectrum from such nanohole arrays, there is usually also a peak at longer wavelengths giving rise to enhanced transmission, particularly at NIR frequencies, which accounts for over half of the solar spectrum.[148,155] The optical properties of the nanohole arrays can be tuned based on the period and shape of the holes, and, if tuned properly, can give rise to enhanced transmission within certain wavelength regimes, which could allow nanohole arrays to be useful as ITO alternatives for organic optoelectronics if designed carefully. However, the usefulness of EOT in optically thin perforated metallic films is sometimes discounted since planar metal films below ~30 nm can already exhibit high transparency.[129] Additionally, whether or not EOT effects are useful in BHJ-OPV devices incorporating plasmonic nanohole array transparent electrodes has yet to be experimentally verified.

Further, when nanohole arrays are filled and coated by absorbers, it has been shown that the metal undergoes an anomalous transparency in a region where the metal should be opaque.[156,157] This transparency, which is separate from the EOT effect, occurs at wavelengths slightly redshifted from the absorption peak of the absorbing material. This phenomenon, called absorption-induced transparency (AIT), is still not fully understood but is proposed to be due to either coupling to an SPP[156] or a change in the imaginary part of the propagation constant of the combined hole-absorber "waveguide."[157] The AIT phenomenon has also not yet been explored for use in BHJ-OPVs, but in cases where nanohole arrays are used as transparent electrodes, AIT could potentially play an important role in increasing the absorption enhancement factor in the active layer. In addition to exhibiting unique optical properties, metallic electrodes consisting of nanohole arrays can exhibit lower resistivity compared to ITO, making them viable transparent plasmonic front electrodes for OPV applications.[45]

Semitransparent or optically thin planar metal electrodes[125–127,158] (formed directly by thermal evaporation) exhibit beneficial optical properties for transparent front electrode applications that can contribute to improved optoelectronic device performance. For example, Neutzner et al. built an inverted P3HT:PCBM solar cell with an ~8-nm thick Ag film which acted as the transparent front electrode and a 100-nm Ag film as the back electrode.[125] The device performance was improved by taking advantage of light trapping due to the resonant nanocavity effect (between the front and back electrode) and the low R_s. In this way, the short-circuit current density was increased by 84% and the power conversion efficiency was doubled compared to a comparable device with a regular ITO transparent front electrode.[125]

Nanostructured multilayers are also an intriguing prospect for harvesting solar energy in BHJ-OPV devices. Super absorbers consisting of metal-insulator-metal (MIM) nanostructures fabricated by Aydin et al. have been shown to result in broadband light absorption over the whole

visible spectrum with an absorbance of 71%.[133] Additionally, opto-fluidic and Raman scattering studies of a "quasi-3D" plasmonic crystal with a polymer layer placed in between a planar gold film and a gold nanohole array together with recessed gold disks indicated significant potential for the use of such multilayer structures as transparent or composite electrodes in OPVs.[135]

For 1-D plasmonic grating transparent electrodes, several optical modes have been shown to be supported: symmetric and antisymmetric SPP MIM modes (TM polarization) as well as photonic MIM waveguide modes (TE polarization),[49,118–120] which could be excited from scattering off of AgNWs,[49] cavity modes,[119] and LSPRs from individual AgNWs.[49] Crossed AgNWs and crossed metallic gratings can also exhibit unique cavity resonances in multilayer formats. Yu et al. have reported the fabrication (using NIL) and optical properties of a double-layer metal grating structure consisting of two layers of Au gratings (each with period of 190 nm) separated by a layer of 200-nm thick PMMA.[159] Compared with single-layer metal wire grid polarizers, Yu et al. suggested that the resonance between the two metal gratings can help control the polarization dependence of transmitted and reflected light from the gratings.[159] Such multilayer structures may be of interest to enhance the polarization-dependent optical properties of transparent plasmonic electrodes. Studies on randomly distributed AgNW networks typically have not reported these types of resonant, waveguide, or SPP modes;[60,61,121–123] rather, the focus of the optical studies has been to maximize transmittance relative to ITO-coated substrates. The shadowing of active layers by NW networks can occur at high area fractions; therefore, in order to maximize the number of connections between NWs while maintaining low area fractions, it is necessary to maximize the aspect ratio of the NWs. Additionally, AgNW meshes for BHJ-OPV applications should ideally maximize haze (i.e., percentage of light forward-scattered by more than 2.5 deg relative to the unscattered incident beam), resulting in an increased optical path length through the active layer, leading to improved active layer absorption.[43,138]

3.2 *Electrical Effects of Plasmonic Transparent Electrodes*

In addition to the broadband, omniacceptance of the PlaCSH-SC described in the previous section, the PlaCSH electrode (for a hole diameter of 175 nm) also exhibited high T (81% peak transmittance) and low R_{sheet} (2.2 $\Omega/\square$), both of which are necessary for replacing ITO.[45] However, although the peak T was high, the overall T ranged from ~55% to 80% across the visible spectrum, which is still quite low compared to that of ITO (>80% across the visible spectrum). Another type of nanohole array fabricated by nanosphere lithography showed an optimized R_{sheet} of 8 $\Omega/\square$ with an average transmittance of 77% from 300 to 1200 nm.[46] Further optimization of the nanohole arrays is necessary to increase T while maintaining the low R_s of the transparent metal films.

One study compared AgNWs on glass and PET substrates with ITO on glass and PET substrates and showed that, although the transmittance was slightly better for ITO/glass and ITO/PET substrates than the AgNW/substrates, and the R_{sheet} was comparable between ITO/glass and AgNW/glass substrates (~10 $\Omega/\square$), the AgNWs/PET had a significantly lower R_{sheet} (13 $\Omega/\square$) than that of the ITO/PET (46 $\Omega/\square$).[61] Further, the AgNWs/PET only showed an increase in the R_{sheet} of ~6% after 1000 bend tests, whereas the R_{sheet} of the ITO/PET increased by ~36% after being bent 1000 times, demonstrating that AgNWs outperformed ITO in terms of mechanical stability for flexible devices.[61]

The surface roughness of AgNW networks is reported to be responsible for low shunt resistances in OPV devices.[124] To correct for this, planarization of the rough electrode surface by means of a thick buffer layer has been proposed.[124] However, regardless of the amount of roughness of the AgNW mesh, the void regions between individual NWs must be filled in order to create a competitive transparent conducting electrode. These void regions act like pores that reduce conductivity and charge extraction properties of the electrode. Ajuria et al. prepared OPVs using a AgNW mesh as the transparent electrode with a thin layer of Ag (5 to 10 nm) sputtered on top of the AgNW mesh, and a buffer layer of ZnO to fill all gaps between AgNWs and create a continuous electrode for charge extraction and collection.[124] This created a quasicontinuous layer that performed as a void-bridging conductor. Their results suggested that a supporting layer is needed between adjacent AgNWs in order to provide the large transverse conductivity needed to collect all of the photogenerated charges.

AgNW arrays and metallic films with nanohole arrays seem to be very promising alternatives to ITO for BHJ-OPV devices. Although Ag is more expensive than In per-gram, NWs can be synthesized and deposited using low-cost, solution-based techniques, hence providing optoelectronic devices fabricated with AgNW transparent electrodes with reduced energy payback times relative to radio-frequency-sputtered ITO electrodes.[160,161]

3.3 *Morphological Effects of Plasmonic Transparent Electrodes*

Since the transparent electrode is often used as the base electrode on which BHJ-OPV devices are fabricated, nanostructured metallic transparent electrodes usually do not influence the morphology of the polymer active layer. However, the morphology of the transparent electrodes can be influenced by plasmonic effects. For instance, a recent study has demonstrated that AgNWs can be welded together by employing their plasmonic absorption, leading to an increase in the local temperature which allowed their junctions to fuse together.[121] In that study, the authors exposed a AgNW network to a tungsten-halogen lamp with a power density of 30 W/cm^2 for 60 s and observed a change from discrete AgNWs before illumination to welded AgNW junctions after illumination. The process was considered self-limiting because the heating and subsequent recrystallization was spatially limited to the junction between AgNWs. This method can be very useful for improving the R_{sheet} of AgNW networks without heating the underlying substrate or active layer. In addition to optical welding, nanosoldering of AgNW networks has also been demonstrated by Mayer rod-coating with a PEDOT:PSS layer [Figs. 10(f) and 10(g)].[123] Upon drying, the PEDOT:PSS coating strongly joined the AgNWs together at their junctions. Long AgNW-PEDOT:PSS composite electrodes exhibited between 80% and 90% T across the visible spectrum with R_{sheet} values of ~25 to 50 $\Omega/\square$, maintaining low R_{sheet} values over 20,000 cyclic bending tests and 5% to 10% stretching.[123]

4 Plasmonic Interlayers

While Interlayers incorporating discrete metallic NPs have been studied extensively in recent years and there are numerous reviews on the topic,[162–167] interlayers consisting of continuous metallic nanostructures, such as the gratings shown in Fig. 3(c) or nanohole arrays, have not been studied as extensively. Typically, when plasmonic electrodes are incorporated into interlayers, the hybrid metallic-interlayer structures serve as both the electron- or hole-selective layer as well as the front transparent electrode. Combined plasmonic interlayer/transparent electrode structures have typically employed 1-D[49,50,168–170] or 2-D[168] gratings. In these cases, since the hybrid plasmonic electrode-interlayer serves as the transparent electrode as well, the devices benefit from both the plasmonic effects (as described in Secs. 2 and 3) and the elimination of ITO. Kang et al. fabricated these types of interlayer structures using NIL with reactive ion etching to break-through the trenches of the grating in the resist, followed by thermal evaporation and subsequent lift-off procedures prior to spin-coating the interlayer material (PEDOT:PSS).[49] For their NW grating structure, the authors observed surface plasmon modes in an MIM structure under TM polarization, as well as broad absorption enhancement in a CuPc/C_{60} bilayer active layer for wavelengths greater than 750 nm over a range of different periods, which the authors attributed to LSPRs from individual NWs.[49] Under TE polarization, the absorption enhancement was attributed to scattering from the NWs coupling light into photonic waveguide modes.[49]

In some instances, plasmonic nanostructures have been embedded in interlayers, in which a front transparent electrode was still employed (typically ITO). These structures have been demonstrated for 1-D gratings,[48,67] circular gratings,[171] nanotriangles,[172,173] nanodisks,[174] and NW arrays.[51] Nanosphere lithography has typically been used to fabricate ordered arrays of nanotriangles on a PEDOT:PSS-coated ITO layer,[172,173] and solution-based AgNWs have been used between the PEDOT:PSS and the P3HT:PCBM layers (also incorporating ITO as the transparent electrode), leading to a 1.18 enhancement factor in the efficiency of conventional devices incorporating these types of plasmonic interlayers.[51] The majority of studies to-date on plasmonic interlayers incorporating continuous metallic nanostructures have been computational, as opposed to studies of interlayers consisting of discrete metallic NPs, which have been both

experimental and computational.[162–167] Further experimental studies on plasmonic electrodes as interlayers are necessary to determine if these structures can be beneficial for enhancing the performance of BHJ-OPVs.

5 Conclusions and Future Directions

A variety of different plasmonic, photonic and plasmonic-photonic hybrid modes supported by plasmonic electrodes have been demonstrated to contribute to improved bulk-heterojunction organic photovoltaic (BHJ-OPV) device performance through increased light trapping and active-layer absorption enhancement. Mode types that have been identified include surface plasmon polaritons, localized surface plasmon resonances, Bloch (i.e., Floquet) mode-coupled SPPs, Wood's anomalies, broadband and resonant Rayleigh scattering, and Fabry–Pérot resonances. From studies to date, it is not apparent that a particular mode type is substantially better for BHJ-OPV device applications than the others. However, depending on the device architecture, placement in the device stack, and active layer material properties, it is clear that certain modes will play a more important role in enhancing the optical properties of devices incorporating plasmonic electrodes. Therefore, the need for a particular type of plasmonic electrode that can support particular mode types should be assessed on a case-by-case basis. Furthermore, parasitic absorption in plasmonic electrodes is omnipresent and must be considered alongside the potential optical benefits of plasmonic electrodes for BHJ-OPV applications.

Electrical and electronic effects caused by plasmonic electrodes such as changes in series or shunt resistance, reduced active layer space-charge effects, shortened charge carried collection lengths, and enhancements in photocurrent beyond the bandgap wavelength of the active layer absorbers are typically only observed experimentally in functioning BHJ-OPV devices, and are challenging to predict using optical simulations alone. Therefore, there is a need for more extensive external quantum efficiency and photocurrent studies, as well as coupled optoelectronic device simulations of BHJ-OPV devices incorporating plasmonic electrodes because optical/photonic effects may not be the only cause of enhancements in device performance parameters. Such studies could aid in designing high-performance, multifunctional plasmonic electrodes for use in BHJ-OPVs. Inverted BHJ-OPV devices benefit significantly, both optically and electrically, from the use of integrated plasmonic back electrodes. Additionally, studies of molecular orientation and crystallinity changes arising from the incorporation of plasmonic electrodes into BHJ-OPV devices are not common. Such studies could help determine if control of the molecular orientation can be used as an approach to further increase BHJ-OPV efficiency enhancement factors beyond those currently observed when incorporating plasmonic electrodes.

Appendix List of Abbreviations of BHJ-OPV Materials

BHJ-OPV: bulk-heterojunction organic photovoltaic
PEDOT:PSS: poly(3,4-ethylenedioxythiophene):poly(styrenesulfonate)
ITO: tin-doped indium oxide
PTB7: poly({4,8-bis[(2-ethylhexyl)oxy]benzo[1,2-*b*:4,5-*b*']dithiophene-2,6-diyl}{3-fluoro-2-[(2-ethylhexyl)carbonyl]thieno[3,4-*b*]thiophenediyl})
$PC_{70}BM$: [6,6]-phenyl-C_{71}-butyric acid methyl ester
PS: polystyrene
PDMS: polydimethylsiloxane
P3HT: poly(3-hexylthiophene-2,5-diyl)
PCBM: [6,6]-phenyl-C_{61}-butyric acid methyl ester
PCDTBT: poly[N-9'-heptadecanyl-2,7-carbazole-*alt*-5,5-(4',7'-di-2-thienyl-2',1',3'-benzothiadiazole)]
PVK: poly(9-vinylcarbazole)
PMMA: poly(methyl methacrylate)
PET: poly(ethylene terephthalate)
APFO Green5: poly[9,9-dioctyl-9*H*-fluorene-*alt*-2,3-bis[4'-(2'-ethylhexyloxy)phenyl]-5,7-di-thiophen-2-yl-thieno[3,4-*b*]pyrazine]

PBDTTT-C-T: poly{[4,8-bis-(2-ethyl-hexyl-thiophene-5-yl)-benzo[1,2-*b*:4,5-*b′*]dithiophene-2,6-diyl]-*alt*-[2-(2′-ethyl-hexanoyl)-thieno[3,4-*b*]thiophen-4,6-diyl]}
PCPDTBT: poly[2,6-(4,4-bis-(2-ethylhexyl)-4*H*-cyclopenta[2,1-*b*;3,4-*b*']dithiophene)-*alt*-4,7(2,1,3-benzothiadiazole)]
PTPTBT: poly({4,4,9,9-tetrakis(4'-hexylphenyl)-2-thiophen-2-yl-benzo[1",2":4,5; 4",5":3',4']dicyclopenta[1,2-*b*:1',2'-*b*']dithiophene} {5,7'-(4'-2-thienyl-2',1',3'-benzothiadiazole)})
ICBA: indene-C_{60} bisadduct
CuPc: copper (II) phthalocyanine
PTCBI: 3,4,9,10-perylenetetracarboxylic bisbenzimidazole

Acknowledgments

This work was supported through funding provided by NSF IGERT Grant No. 0903661, NSF Grant No. DMR-1309459, and Rutgers Aresty Undergraduate Research Center.

References

1. H. A. Atwater and A. Polman, "Plasmonics for improved photovoltaic devices," *Nat. Mater.* **9**, 205–213 (2010).
2. V. E. Ferry, J. N. Munday, and H. A. Atwater, "Design considerations for plasmonic photovoltaics," *Adv. Mater.* **22**, 4794–4808 (2010).
3. S. Pillai and M. A. Green, "Plasmonics for photovoltaic applications," *Sol. Energy Mater. Sol. Cells* **94**, 1481–1486 (2010).
4. V. E. Ferry, A. Polman, and H. A. Atwater, "Modeling light trapping in nanostructured solar cells," *ACS Nano* **5**, 10055–10064 (2011).
5. J. N. Munday and H. A. Atwater, "Large integrated absorption enhancement in plasmonic solar cells by combining metallic gratings and antireflection coatings," *Nano Lett.* **11**, 2195–2201 (2011).
6. M. A. Green and S. Pillai, "Harnessing plasmonics for solar cells," *Nat. Photonics* **6**, 130–132 (2012).
7. F. J. Beck, S. Mokkapati, and K. R. Catchpole, "Plasmonic light-trapping for Si solar cells using self-assembled, Ag nanoparticles," *Prog. Photovoltaics* **18**, 500–504 (2010).
8. F. J. Beck et al., "Asymmetry in photocurrent enhancement by plasmonic nanoparticle arrays located on the front or on the rear of solar cells," *Appl. Phys. Lett.* **96**, 033113 (2010).
9. V. E. Ferry et al., "Light trapping in ultrathin plasmonic solar cells," *Opt. Express* **18**, A238–A245 (2010).
10. E. Stratakis and E. Kymakis, "Nanoparticle-based plasmonic organic photovoltaic devices," *Mater. Today* **16**(4), 133–146 (2013).
11. M. Notarianni et al., "Plasmonic effect of gold nanoparticles in organic solar cells," *Sol. Energy* **106**, 23–37 (2014).
12. Q. Gan, F. J. Bartoli, and Z. H. Kafafi, "Plasmonic-enhanced organic photovoltaics: breaking the 10% efficiency barrier," *Adv. Mater.* **25**(17), 2385–2396 (2013).
13. A. Uddin and X. Yang, "Surface plasmonic effects on organic solar cells," *J. Nanosci. Nanotechnol.* **14**, 1099–1119 (2014).
14. C.-H. Chou and F.-C. Chen, "Plasmonic nanostructures for light trapping in organic photovoltaic devices," *Nanoscale* **6**(15), 8444–8458 (2014).
15. W. C. H. Choy, "The emerging multiple metal nanostructures for enhancing the light trapping of thin film organic photovoltaic cells," *Chem. Commun.* **50**(81), 11984–11993 (2014).
16. F. Zhang et al., "Recent development of the inverted configuration organic solar cells," *Sol. Energy Mater. Sol. Cells* **95**, 1785–1799 (2011).
17. S. K. Hau, H.-L. Yip, and A. K.-Y. Jen, "A review on the development of the inverted polymer solar cell architecture," *Polymer Rev.* **50**, 474–510 (2010).
18. M. Jørgensen et al., "Stability of polymer solar cells," *Adv. Mater.* **24**, 580–612 (2012).

19. M. P. de Jong, L. J. van IJzendoorn, and M. J. de Voigt, "Stability of the interface between indium-tin-oxide and poly(3,4-ethylenedioxythiophene)/poly(styrenesulfonate) in polymer light-emitting diodes," *Appl. Phys. Lett.* **77**, 2255–2257 (2000).
20. M. T. Lloyd et al., "Impact of contact evolution on the shelf life of organic solar cells," *J. Mater. Chem.* **19**, 7638–7642 (2009).
21. W. Cai, X. Gong, and Y. Cao, "Polymer solar cells: recent development and possible routes for improvement in the performance," *Sol. Energy Mater. Sol. Cells* **94**, 114–127 (2010).
22. M.-C. Chen et al., "Small organic additive to improve the charge separation in an inverted bulk heterojunction organic photovoltaic," *Org. Electron.* **13**, 2702–2708 (2012).
23. F.-C. Chen et al., "Flexible polymer photovoltaic devices prepared with inverted structures on metal foils," *IEEE Electron. Device Lett.* **30**, 727–729 (2009).
24. J. Ajuria et al., "Inverted ITO-free organic solar cells based on p and n semiconducting oxides. New designs for integration in tandem cells, top or bottom detecting devices, and photovoltaic windows," *Energy Environ. Sci.* **4**, 453–458 (2011).
25. M. A. Green et al., "Solar cell efficiency tables (version 44)," *Prog. Photovoltaics* **22**, 701–710 (2014).
26. Press release: Heliatek GmbH, "Neuer weltrekord für organische solarzellen: Heliatek behauptet sich mit 12% zelleffizienz als technologieführer," (2013).
27. Z. He et al., "Enhanced power-conversion efficiency in polymer solar cells using an inverted device structure," *Nat. Photonics* **6**, 591–595 (2012).
28. S. A. Maier, *Plasmonics Fundamentals and Applications*, Springer Science+Business Media LLC, New York, USA (2007).
29. M. G. Deceglie et al., "Design of nanostructured solar cells using coupled optical and electrical modeling," *Nano. Lett.* **12**(6), 2894–900 (2012).
30. X. H. Li et al., "Efficient inverted polymer solar cells with directly patterned active layer and silver back grating," *J. Phys. Chem. C* **116**, 7200–7206 (2012).
31. J. You et al., "Surface plasmon and scattering-enhanced low-bandgap polymer solar cell by a metal grating back electrode," *Adv. Energy Mater.* **2**, 1203–1207 (2012).
32. X. Li et al., "Dual plasmonic nanostructures for high performance inverted organic solar cells," *Adv. Mater.* **24**(22), 3046–3052 (2012).
33. B. Niesen et al., "Plasmonic efficiency enhancement of high performance organic solar cells with a nanostructured rear electrode," *Adv. Energy Mater.* **3**, 145–150 (2013).
34. W. Bai et al., "Broadband short-range surface plasmon structures for absorption enhancement in organic photovoltaics," *Opt. Express* **18**(S4), A620–A630 (2010).
35. W. Bai et al., "Double plasmonic structure design for broadband absorption enhancement in molecular organic solar cells," *J. Photonics Energy* **1**, 011121 (2011).
36. W. E. I. Sha, X. Li, and W. C. H. Choy, "Breaking the space charge limit in organic solar cells by a novel plasmonic-electrical concept," *Sci. Rep.* **4**, 6236 (2014).
37. Y. Liu et al., "Polarization-diverse light absorption enhancement in organic photovoltaic structures with one-dimensional, long-pitch metallic gratings: design and experiment," *Appl. Phys. Lett.* **101**, 233904 (2012).
38. W. Vervisch et al., "Optical-electrical simulation of organic solar cells: influence of light trapping by photonic crystal and ZnO spacer on electrical characteristics," *J. Appl. Phys.* **111**, 094506 (2012).
39. R. G. Sabat, M. J. L. Santos, and P. Rochon, "Surface plasmon-induced band gap in the photocurrent response of organic solar cells," *Int. J. Photoenergy* **2010**, 698718 (2010).
40. Y.-S. Hsiao et al., "Facile transfer method for fabricating light-harvesting systems for polymer solar cells," *J. Phys. Chem. C* **115**, 11864–11870 (2011).
41. D. M. O'Carroll et al., "Surface plasmon assisted absorption in conjugated polymer thin films and devices," in *25th European Photovoltaic Solar Energy Conference and Exhibition*, pp. 834–836 (2010).
42. C. T. Nemes et al., "Absorption and scattering effects by silver nanoparticles near the interface of organic/inorganic semiconductor tandem films," *J. Nanopart. Res.* **15**, 1801 (2013).

43. S. Ye et al., "Metal nanowire networks: the next generation of transparent conductors," *Adv. Mater.* **26**(39), 6670–6687 (2014).
44. D. S. Hecht, L. Hu, and G. Irvin, "Emerging transparent electrodes based on thin films of carbon nanotubes, graphene, and metallic nanostructures," *Adv. Mater.* **23**, 1482–1513 (2011).
45. S. Y. Chou and W. Ding, "Ultrathin, high-efficiency, broad-band, omni-acceptance, organic solar cells enhanced by plasmonic cavity with subwavelength hole array," *Opt. Express* **21**(S1), A60–A76 (2013).
46. A. J. Morfa et al., "Transparent metal electrodes from ordered nanosphere arrays," *J. Appl. Phys.* **114**, 054502 (2013).
47. L. Hu et al., "Scalable coating and properties of transparent, flexible, silver nanowire electrodes," *ACS Nano* **4**(5), 2955–2963 (2010).
48. M. A. Sefunc, A. K. Okyay, and H. V. Demir, "Plasmonic backcontact grating for P3HT: PCBM organic solar cells enabling strong optical absorption increased in all polarizations," *Opt. Express* **19**(15), 14200–14209 (2011).
49. M.-G. Kang et al., "Efficiency enhancement of organic solar cells using transparent plasmonic Ag nanowire electrodes," *Adv. Mater.* **22**(39), 4378–4383 (2010).
50. C. Min et al., "Enhancement of optical absorption in thin-film organic solar cells through the excitation of plasmonic modes in metallic gratings," *Appl. Phys. Lett.* **96**, 133302 (2010).
51. Y. Yang et al., "Enhancement of short-circuit current density in polymer bulk heterojunction solar cells comprising plasmonic silver nanowires," *Appl. Phys. Lett.* **104**, 123302 (2014).
52. Y. Liu et al., "Balance between light trapping and charge carrier collection: electrophotonic optimization of organic photovoltaics with ridge-patterned back electrodes," *J. Appl. Phys.* **113**, 244503 (2013).
53. D. Lu et al., "Interaction of two plasmon modes in the organic photovoltaic devices with patterned back-electrode," *Appl. Phys. Lett.* **102**, 241114 (2013).
54. X. Li et al., "Polarization-independent efficiency enhancement of organic solar cells by using 3-dimensional plasmonic electrode," *Appl. Phys. Lett.* **102** 153304 (2013).
55. A. E. Ostfeld and D. Pacifici, "Plasmonic concentrators for enhanced light absorption in ultrathin film organic photovoltaics," *Appl. Phys. Lett.* **98**, 113112 (2011).
56. A. Abass et al., "Angle insensitive enhancement of organic solar cells using metallic gratings," *J. Appl. Phys.* **109**, 023111 (2011).
57. D. M. N. M. Dissanayake, B. Roberts, and P.-C. Ku, "Plasmonic backscattering enhanced inverted photovoltaics," *Appl. Phys. Lett.* **99**, 113306 (2011).
58. R. R. Grote et al., "Morphology-dependent light trapping in thin-film organic solar cells," *Opt. Express* **21**(S5), A847–A863 (2013).
59. E. Lee and C. Kim, "Analysis and optimization of surface plasmon-enhanced organic solar cells with a metallic crossed grating electrode," *Opt. Express* **20**(S5), A740–A753 (2012).
60. J.-Y. Lee et al., "Semitransparent organic photovoltaic cells with laminated top electrode," *Nano Lett.* **10**(4), 1276–1279 (2010).
61. M. Song et al., "Highly efficient and bendable organic solar cells with solution-processed silver nanowire electrodes," *Adv. Funct. Mater.* **23**, 4177–4184 (2013).
62. H.-K. Park et al., "Characteristics of indium-free GZO/Ag/GZO and AZO/Ag/AZO multilayer electrode grown by dual target DC sputtering at room temperature for low-cost organic photovoltaics," *Sol. Energy Mater. Sol. Cells* **93**, 1994–2002 (2009).
63. M. Kohlstädt et al., "Inverted ITO- and PEDOT:PSS-free polymer solar cells with high power conversion efficiency," *Sol. Energy Mater. Sol. Cells* **117**, 98–102 (2013).
64. J.-A. Jeong and H.-K. Kim, "Low resistance and highly transparent ITO-Ag-ITO multilayer electrode using surface plasmon resonance of Ag layer for bulk-heterojunction organic solar cells," *Sol. Energy Mater. Sol. Cells* **93**, 1801–1809 (2009).
65. Y.-S. Park et al., "Comparative investigation of transparent ITO/Ag/ITO and ITO/Cu/ITO electrodes grown by dual-target DC sputtering for organic photovoltaics," *J. Electrochem. Soc.* **156**(7), H588–H594 (2009).

66. K. Tvingstedt and O. Inganäs, "Electrode grids for ITO-free organic photovoltaic devices," *Adv. Mater.* **19**, 2893–2897 (2007).
67. M. A. Sefunc, A. K. Okayay, and H. V. Demir, "Volumetric plasmonic resonator architecture for thin-film solar cells," *Appl. Phys. Lett.* **98**, 093117 (2011).
68. H. Shen and B. Maes, "Combined plasmonic gratings in organic solar cells," *Opt. Express* **19**(S6), A1202–A1210 (2011).
69. B. Zeng et al., "Polymeric photovoltaics with various metallic plasmonic nanostructures," *J. Appl. Phys.* **113**, 063109 (2013).
70. L. J. Guo, "Nanoimprint lithography: methods and material requirements," *Adv. Mater.* **19**, 495–513 (2007).
71. N. Kooy et al., "A review of roll-to-roll nanoimprint lithography," *Nanoscale Res. Lett.* **9**, 320 (2014).
72. S. H. Ahn and L. J. Guo, "High-speed roll-to-roll nanoimprint lithography on flexible plastic substrates," *Adv. Mater.* **20**, 2044–2049 (2008).
73. A. Baba et al., "Grating-coupled surface plasmon enhanced short-circuit current in organic thin-film photovoltaic cells," *ACS Appl. Mater. Interfaces* **3**(6), 2080–2084 (2011).
74. R. Meier et al., "Efficiency-improved organic solar cells based on plasticizer assisted soft embossed PEDOT:PSS layers," *Phys. Chem. Chem. Phys.* **14**(43), 15088–15098 (2012).
75. L. Müller-Meskamp et al., "Efficiency enhancement of organic solar cells by fabricating periodic surface textures using direct laser interference patterning," *Adv. Mater.* **24**, 906–910 (2012).
76. W. Wang et al., "High-efficiency, broad-band and wide-angle optical absorption in ultra-thin organic photovoltaic devices," *Opt. Express* **22**(S2), A376–A385 (2014).
77. S. Y. Chou, P. R. Krauss, and P. J. Renstrom, "Nanoimprint lithography," *J. Vac. Sci. Technol. B* **14**(6), 4129–4133 (1996).
78. S. Y. Chou, P. R. Krauss, and P. J. Renstrom, "Imprint lithography with 25-nanometer resolution," *Science* **272**, 85–87 (1996).
79. C. Lertvachirapaiboon et al., "Solution-based fabrication of gold grating film for use as a surface plasmon resonance sensor chip," *Sensors Actuators B* **173**, 316–321 (2012).
80. T. Bailey et al., "Step and flash imprint lithography: template surface treatment and defect analysis," *J. Vac. Sci. Technol. B* **18**(6), 3572–3577 (2000).
81. M. D. Austin et al., "Fabrication of 5 nm linewidth and 14 nm pitch features by nano-imprint lithography," *Appl. Phys. Lett.* **84**(26), 5299–5301 (2004).
82. K. Tvingstedt et al., "Surface plasmon increase absorption in polymer photovoltaic cells," *Appl. Phys. Lett.* **91**, 113514 (2007).
83. M. Aryal, K. Trivedi, and W. W. Hu, "Nano-confinement induced chain alignment in ordered P3HT nanostructures defined by nanoimprint lithography," *ACS Nano* **3**(10), 3085–3090 (2009).
84. H. Hlaing et al., "Nanoimprint-induced molecular orientation in semiconducting polymer nanostructures," *ACS Nano* **5**(9), 7532–7538 (2011).
85. J. B. Kim et al., "Wrinkles and deep folds as photonic structures in photovoltaics," *Nat. Photonics* **6**, 327–332 (2012).
86. J. W. Menezes et al., "Large area fabrication of periodic arrays of nanoholes in metal films and their application in biosensing and plasmonic-enhanced photovoltaics," *Adv. Funct. Mater.* **20**, 3918–3924 (2010).
87. V. E. Ferry et al., "Improved red-response in thin film a-Si:H solar cells with soft imprinted plasmonic back reflectors," *Appl. Phys. Lett.* **95**, 183503 (2009).
88. J. C. Hulteen and R. P. Van Duyne, "Nanosphere lithography: a materials general fabrication process for periodic particle array surfaces," *J. Vac. Sci. Technol. A* **13**(3), 1553–1558 (1995).
89. C. L. Haynes and R. P. Van Duyne, "Nanosphere lithography: a versatile nanofabrication tool for studies of size-dependent nanoparticle optics," *J. Phys. Chem. B* **105**, 5599–5611 (2001).
90. H. Fredriksson et al., "Hole-mask colloidal lithography," *Adv. Mater.* **19**, 4297–4302 (2007).

91. M. R. Gonçalves et al., "Plasmonic nanostructures fabricated using nanosphere-lithography, soft-lithography and plasma etching," *Beilstein J. Nanotechnol.* **2**, 448–458 (2011).
92. S. Cataldo et al., "Hole-mask colloidal nanolithography for large-area low-cost metamaterials and antenna-assisted surface-enhanced infrared absorption substrates," *ACS Nano* **6**(1), 979–985 (2012).
93. P. W. Flanigan et al., "A generalized "cut and projection" algorithm for the generation of quasiperiodic plasmonic concentrators for high efficiency ultra-thin film photovoltaics," *Opt. Express* **21**(3), 2757–2776 (2013).
94. M. W. Knight et al., "Photodetection with active optical antennas," *Science* **332**, 702–704 (2011).
95. F. Wang and N. A. Melosh, "Plasmonic energy collection through hot carrier extraction," *Nano Lett.* **11**, 5426–5430 (2011).
96. H. Chalabi, D. Schoen, and M. L. Brongersma, "Hot-electron photodetection with a plasmonic nanostripe antenna," *Nano Lett.* **14**, 1374–1380 (2014).
97. C. Clavero, "Plasmon-induced hot-electron generation at nanoparticle/metal-oxide interfaces for photovoltaic and photocatalytic devices," *Nat. Photonics* **8**, 95–103 (2014).
98. A. J. Leenheer et al., "Solar energy conversion via hot electron internal photoemission in metallic nanostructures: efficiency estimates," *J. Appl. Phys.* **115**, 134301 (2014).
99. T. P. White and K. R. Catchpole, "Plasmon-enhanced internal photoemission for photovoltaics: theoretical efficiency limits," *Appl. Phys. Lett.* **101**, 073905 (2012).
100. M. Campoy-Quiles et al., "Advanced ellipsometric characterization of conjugated polymer films," *Adv. Funct. Mater.* **24**, 2116–2134 (2014).
101. A. J. Morfa et al., "Optical characterization of pristine poly(3-hexyl thiophene) films," *J. Polymer Sci.* **49**, 186–194 (2011).
102. C. M. Ramsdale and N. C. Greenham, "The optical constants of emitter and electrode materials in polymer light-emitting diodes," *J. Phys. D* **36**, L29–L34 (2003).
103. C. M. Ramsdale and N. C. Greenham, "Ellipsometric determination of anisotropic optical constants in electroluminescent conjugated polymers," *Adv. Mater.* **14**(3), 212–215 (2002).
104. M. Tammer and A. P. Monkman, "Measurement of the anisotropic refractive indices of spin cast thin poly(2-methoxy-5-(2'-ethyl-hexyloxy)-*p*-phenylenevinylene) (MEH-PPV) films," *Adv. Mater.* **14**(3), 210–212 (2002).
105. M. Campoy-Quiles et al., "On the determination of anisotropy in polymer thin films: a comparative study of optical techniques," *Physica Status Solidi C* **5**(5), 1270–1273 (2008).
106. D. M. O'Carroll, C. E. Hofmann, and H. A. Atwater, "Conjugated polymer/metal nanowire heterostructure plasmonic antennas," *Adv. Mater.* **22**(11), 1223–1227 (2010).
107. D. M. O'Carroll et al., "Metal-polymer-metal split-dipole nanoantennas," *Adv. Mater.* **24**(23), OP136–OP142 (2012).
108. M. R. Hammond et al., "Molecular order in high-efficiency polymer/fullerene bulk heterojunction solar cells," *ACS Nano* **5**(10), 8248–8257 (2011).
109. M. G. Kang et al., "Toward low-cost, high-efficiency, and scalable organic solar cells with transparent metal electrode and improved domain morphology," *IEEE J. Sel. Top. Quantum Electron.* **16**(6), 1807–1820 (2010).
110. K. Ellmer, "Past achievements and future challenges in the development of optically transparent electrodes," *Nat. Photonics* **6**, 809–817 (2012).
111. K. S. Kim et al., "Large scale pattern growth of graphene films for stretchable transparent electrodes," *Nature* **457**, 706–710 (2009).
112. G. Eda and M. Chhowalla, "Chemically derived graphene oxide: towards large-area thin-film electronics and optoelectronics." *Adv. Mater.* **22**, 2392–2415 (2010).
113. A. Shimoni, S. Axoubel, and S. Magdassi, "Inkjet printing of flexible high-performance carbon nanotube transparent conductive films by 'coffee ring effect,'" *Nanoscale* **6**, 11084–11089 (2014).
114. M. Layani, A. Kamyshny, and S. Magdassi, "Transparent conductors composed of nanomaterials," *Nanoscale* **6**, 5581–5591 (2014).

115. W. A. Luhman et al., "Self-assembled plasmonic electrodes for high-performance organic photovoltaic cells," *Appl. Phys. Lett.* **99**, 103306 (2011).
116. J. Zhu et al., "Metallic nanomesh electrodes with controllable optical properties for organic solar cells," *Appl. Phys. Lett.* **100**, 143109 (2012).
117. T. H. Reilly, III et al., "Surface-plasmon enhanced transparent electrodes in organic photovoltaics," *Appl. Phys. Lett.* **92**, 243304 (2008).
118. P. B. Catrysse and S. Fan, "Nanopatterned metallic films for use as transparent conductive electrodes in optoelectronic devices," *Nano Lett.* **10**, 2944–2949 (2010).
119. N. C. Lindquist et al., "Plasmonic nanocavity arrays for enhanced efficiency in organic photovoltaic cells," *Appl. Phys. Lett.* **93**, 123308 (2008).
120. Z. Ye et al., "Broadband light absorption enhancement in polymer photovoltaics using metal nanowall gratings as transparent electrodes," *Opt. Express* **20**(11), 12213–12221 (2012).
121. E. C. Garnett et al., "Self-limited plasmonic welding of silver nanowire junctions," *Nat. Mater.* **11**(3), 241–249 (2012).
122. W. Gaynor, J.-Y. Lee, and P. Peumans, "Fully solution-processed inverted polymer solar cells with laminated nanowire electrodes," *ACS Nano* **4**(1), 30–34 (2010).
123. J. Lee et al., "Room-temperature nanosoldering of a very long metal nanowire network by conducting-polymer-assisted joining for a flexible touch-panel application," *Adv. Funct. Mater.* **23**, 4171–4176 (2013).
124. J. Ajuria et al., "Insights on the working principles of flexible and efficient ITO-free organic solar cells based on solution processed Ag nanowire electrodes," *Sol. Energy Mater. Sol. Cells* **102**, 148–152 (2012).
125. S. Neutzner et al., "Control of light absorption in organic solar cells using semi-transparent metal electrodes," *Proc. SPIE* **8811**, 881119 (2013).
126. N. P. Sergeant et al., "Design of transparent anodes for resonant cavity enhanced light harvesting in organic solar cells," *Adv. Mater.* **24**, 728–732 (2012).
127. J. F. Salinas et al., "Optical design of transparent thin metal electrodes to enhance in-coupling and trapping of light in flexible polymer solar cells," *Adv. Mater.* **24**, 6362–6367 (2012).
128. W. Yu et al., "Effects of the optical microcavity on the performances of ITO-free polymer solar cells with WO3/Ag/WO3 transparent electrode," *Sol. Energy Mater. Sol. Cells* **100**, 226–230 (2012).
129. C. Genet and T. W. Ebbesen, "Light in tiny holes," *Nature* **445**, 39–46 (2007).
130. H. F. Ghaemi et al., "Surface plasmons enhance optical transmission through subwavelength holes," *Phys. Rev. B* **58**(11), 6779–6782 (1998).
131. W. L. Barnes et al., "Surface plasmon polaritons and their role in the enhanced transmission of light through periodic arrays of subwavelength holes in a metal film," *Phys. Rev. Lett.* **92**(10), 107401 (2004).
132. Y. M. Chi et al., "Optimizing surface plasmon resonance effects on finger electrodes to enhance the efficiency of silicon-based solar cells," *Energy Environ. Sci.* **6**, 935–942 (2013).
133. K. Aydin et al., "Broadband polarization-independent resonant light absorption using ultrathin plasmonic super absorbers," *Nat. Commun.* **2**, 517 (2011).
134. W. Ding et al., "Plasmonic nanocavity organic light-emitting diode with significantly enhanced light extraction, contrast, viewing angle, brightness, and low-glare," *Adv. Funct. Mater.* **24**(40), 6329–6339 (2014).
135. D. Chanda et al., "Coupling of plasmonic and optical cavity modes in quasi-three-dimensional plasmonic crystals," *Nat. Commun.* **2**, 479 (2011).
136. Y. Ahn, Y. Jeong, and Y. Lee, "Improved thermal oxidation stability of solution-processable silver nanowire transparent electrode by reduced graphene oxide," *ACS Appl. Mater. Interfaces* **4**(12), 6410–6414 (2012).
137. T. Z. Oo et al., "Ultrafine gold nanowire networks as plasmonic antennae in organic photovoltaics," *J. Phys. Chem. C* **116**, 6453–6458 (2012).
138. J. Krantz et al., "Spray-coated silver nanowires as top electrode layer in semitransparent P3HT:PCBM-based organic solar cell devices," *Adv. Funct. Mater.* **23**, 1711–1717 (2013).

139. Y.-J. Kang et al., "Progress towards fully spray-coated semitransparent inverted organic solar cells with a silver nanowire electrode," *Org. Electron.* **15**, 2173–2177 (2014).
140. S.-E. Park et al., "Fabrication of silver nanowire transparent electrodes using electrohydrodynamic spray deposition for flexible organic solar cells," *J. Mater. Chem. A* **1**, 14286–14293 (2013).
141. M. Fan, G. F. S. Andrade, and A. G. Brolo, "A review on the fabrication of substrates for surface enhanced Raman spectroscopy and their applications in analytical chemistry," *Anal. Chem. Acta* **693**, 7–25 (2011).
142. R. Gordon et al., "A new generation of sensors based on extraordinary optical transmission," *Acc. Chem. Res.* **41**(8), 1049–1057 (2008).
143. H. Im et al., "Template-stripped smooth Ag nanohole array with silica shells for surface plasmon resonance biosensing," *ACS Nano* **5**(8), 6244–6253 (2011).
144. C. Battagila et al., "Light trapping in solar cells: can periodic beat random?," *ACS Nano* **6**(3), 2790–2797 (2012).
145. J. Biener et al., "Nanoporous plasmonic metamaterials," *Adv. Mater.* **20**, 1211–1217 (2008).
146. H.-A. Chen et al., "Plasmonic properties of a nanoporous gold film investigated by far-field and near-field optical techniques," *J. Appl. Phys.* **110**, 054302 (2011).
147. T. W. Ebbesen et al., "Extraordinary optical transmission through subwavelength hole arrays," *Nature* **391**, 667–669 (1998).
148. S. G. Rodrigo, "Extraordinary optical transmission," Chapter 2 in *Optical Properties of Nanostructured Metallic Systems Studied with the Finite-Difference Time-Domain Method*, pp. 37–75, Springer-Verlag, Berlin Heidelberg (2012).
149. A. Degiron et al., "Effects of hole depth on enhanced light transmission through subwavelength hole arrays," *Appl. Phys. Lett.* **81**, 4327–4329 (2002).
150. S. G. Rodrigo et al., "Extraordinary optical transmission through hole arrays in optically thin metal films," *Opt. Lett.* **34**, 4–6 (2009).
151. L. Martin-Moreno et al., "Theory of extraordinary optical transmission through subwavelength hole arrays," *Phys. Rev. Lett.* **86**, 1114–1117 (2001).
152. N. Bonod et al., "Resonant optical transmission through thin metallic films with and without holes," *Opt. Express* **11**, 482–490 (2003).
153. J. Braun et al., "Optical transmission through subwavelength hole arrays in ultrathin metal films," *Phys. Rev. B* **84**, 155419 (2011).
154. J. Braun et al., "How holes can obscure the view: suppressed transmission through an ultrathin metal film by a subwavelength hole array," *Phys. Rev. Lett.* **103**, 203901 (2009).
155. G. Behera et al., "Enhanced broadband transmission through structured plasmonic thin films for transparent electrodes," *J. Nanophotonics* **8**, 083889 (2014).
156. J. A. Hutchison et al., "Absorption-induced transparency," *Angew. Chem. Int. Ed.* **50**, 2085–2089 (2011).
157. S. G. Rodrigo, F. J. García-Vidal, and L. Martín-Moreno, "Theory of absorption-induced transparency," *Phys. Rev. B* **88**, 155126 (2013).
158. S. Vedraine et al., "Optical characterization of organic blend films integrating metallic nanoparticles," *Sol. Energy Mater. Sol. Cells* **102**, 31–35 (2012).
159. Z. Yu et al., "Reflective polarizer based on a stacked double-layer subwavelength metal grating structure fabricated using nanoimprint lithography," *Appl. Phys. Lett.* **77**(7), 927–929 (2000).
160. C. J. M. Emmott, A. Urbina, and J. Nelson, "Environmental and economic assessment of ITO-free electrodes for organic solar cells," *Sol. Energy Mater. Sol. Cells* **97**, 14–21 (2012).
161. N. Espinosa et al., "Solar cells with one-day energy payback for the factories of the future," *Energy Environ. Sci.* **5**, 5117–5132 (2012).
162. S.-W. Baek et al., "Plasmonic forward scattering effect in organic solar cells: a powerful optical engineering method," *Sci. Rep.* **3**, 1726 (2013).
163. H. Choi et al., "Versatile surface plasmon resonance of carbon-dot-supported silver nanoparticles in polymer optoelectronic devices," *Nat. Photonics* **7**, 732–738 (2013).
164. H. L. Gao et al., "Efficiency enhancement of polymer solar cells by localized surface plasmon of Au nanoparticles," *J. Appl. Phys.* **114**, 163102 (2013).

165. W. Jiang, M. Salvador, and S. T. Dunham, "Combined three-dimensional electromagnetic and device modeling of surface plasmon-enhanced organic solar cells incorporating low aspect ratio silver nanoprisms," *Appl. Phys. Lett.* **103**, 183303 (2013).
166. X. Yang et al., "High-efficiency polymer solar cells achieved by doping plasmonic metallic nanoparticles into dual charge selecting interfacial layers to enhance light trapping," *Adv. Energy Mater.* **3**, 666–673 (2013).
167. A. Uddin and X. Yang, "Surface plasmon enhanced organic solar cell with different silver nanosphere sizes," *J. Nanosci. Nanotechnol.* **14**, 1–9 (2014).
168. I. Kim et al., "Optical design of transparent metal grids for plasmonic absorption enhancement in ultrathin organic solar cells," *Opt. Express* **21**(S4), A669–A676 (2013).
169. S. Lee et al., "Embedding metal electrodes in thick active layers for ITO-free plasmonic organic solar cells with improved performance," *Opt. Express* **22**(S4), A1145–A1152 (2014).
170. Y. Long, Y. Li, and R. Su, "Simultaneously improving optical absorption of both transverse-electric polarized and transverse-magnetic polarized light for organic solar cells with Ag grating used as transparent electrode," *AIP Adv.* **4**, 087143 (2014).
171. N.-F. Chiu et al., "Plasmonic circular nanostructure for enhanced light absorption in organic solar cells," *Int. J. Photoenergy* **2013**, 502576 (2013).
172. B. Wu et al., "Efficiency enhancement in bulk-heterojunction solar cells integrated with large-area Ag nanotriangle arrays," *J. Phys. Chem. C* **116**, 14820–14825 (2012).
173. A. Kirkeminde et al., "Surface-passivated plasmonic nano-pyramids for bulk heterojunction solar cell photocurrent enhancement," *Nanoscale* **4**(15), 4421–4425 (2012).
174. B. Wu et al., "Resonant aluminum nanodisk array for enhanced tunable broadband light trapping in ultrathin bulk heterojunction organic photovoltaic devices," *Plasmonics* **7**, 677–684 (2012).

Christopher Petoukhoff received his BS degrees in physics and chemistry from the University of the Sciences in Philadelphia in 2011. He is currently a PhD candidate in the Department of Materials Science and Engineering at Rutgers University. His research is focused on computationally and empirically designing multifunctional plasmonic back electrodes to improve the efficiency of polymer-based solar cells through tailoring the optical and electronic properties of the electrodes.

Zeqing Shen received her BS degree in chemistry from the University of Science and Technology of China in 2012. She is currently a PhD candidate in the Department of Chemistry and Chemical Biology at Rutgers University. Her work is focused on conjugated polymer chain alignment, photophysics, and electrical properties in nanoporous metal films.

Manika Jain is currently a senior undergraduate in the Department of Materials Science and Engineering at Rutgers University. Over the past 3 years she has carried out research on the solution-based fabrication and optoelectronic characterization of Ag nanowire-ZnO nanoparticle multilayers for use as solution-deposited transparent conducting electrodes on hydrophobic conjugated polymer active layers.

AiMei Chang is currently a senior undergraduate in the Department of Materials Science and Engineering at Rutgers University. She is carrying out a senior thesis research project on employing nanoimprint lithography to fabricate one- and two-dimensional metallic grating electrodes for integration into organic photovoltaic devices. She has served as the secretary to Rutgers' SPIE student chapter for the past year.

Deirdre M. O'Carroll has been an assistant professor in materials science and engineering and chemistry at Rutgers University since 2011. She received her PhD degree in microelectronic engineering from University College Cork in 2008. From 2007 to 2009, she was a postdoctoral researcher in plasmonics at California Institute of Technology, and in 2010 she completed an International Marie Curie Fellowship at University of Strasbourg and CNRS. She specializes in photonic nanostructures, plasmonics, photonics for energy, conjugated polymers, and organic optoelectronics.